Light transport in biological tissue based on the simplified spherical harmonics equations

Alexander D. Klose [a,*], Edward W. Larsen [b]

[a] *Department of Radiology, Columbia University, New York, NY 10032, USA*
[b] *Department of Nuclear Engineering and Radiological Sciences, University of Michigan, Ann Arbor, MI 48109, USA*

Abstract

In this work, we demonstrate the validity of the simplified spherical harmonics equations to approximate the more complicated equation of radiative transfer for modeling light propagation in biological tissue. We derive the simplified spherical harmonics equations up to order $N = 7$ for anisotropic scattering and partially reflective boundary conditions. We compare numerical results with diffusion and discrete ordinates transport solutions. We find that the simplified spherical harmonics methods significantly improve the diffusion solution in transport-like domains with high absorption and small geometries, and are computationally less expensive than the discrete ordinates transport method. For example, the simplified P_3 method is approximately two orders of magnitude faster than the discrete ordinates transport method, but only 2.5 times computationally more demanding than the diffusion method. We conclude that the simplified spherical harmonics methods can accurately model light propagation in small tissue geometries at visible and near-infrared wavelengths, yielding transport-like solutions with only a fraction of the computational cost of the transport calculation.
© 2006 Elsevier Inc. All rights reserved.

1. Introduction

The equation of radiative transfer (ERT) has successfully been used as a standard model for describing light transport in scattering media. However, providing solutions to the ERT is a major endeavor and remains a challenging task in the fields of tissue optics and radiological sciences. In general, analytical solutions to the ERT cannot be found for biological tissue with spatially nonuniform scattering and absorption properties and curved tissue geometries. Instead, approximations to the ERT, such as the discrete ordinates (S_N) and spherical harmonics (P_N) equations, have been established to overcome the constraints for directly solving

* Corresponding author. Tel.: +1 212 854 5868; fax: +1 212 854 8725.
E-mail addresses: ak2083@columbia.edu (A.D. Klose), edlarsen@umich.edu (E.W. Larsen).

the ERT. A low-order P_N approximation, such as the diffusion (P_1) equation, can be solved numerically for problems with optical tissue properties at near-infrared wavelengths constituting diffusive regimes. Many numerical techniques are available and have been employed for the diffusion approximation. Higher-order P_N equations cover also transportive properties of light propagation in tissues, e.g. when strong light absorption or small geometries are present. However, these equations are complicated and computationally demanding, and therefore are not widely-used in tissue optics. In this paper, we propose a simplified spherical harmonics (SP_N) method for tissue optics, which significantly improves the diffusion approximation, but is much less computationally expensive than solving the full P_N or S_N equations. The SP_N equations can be used for solving light propagation problems at visible and near-infrared wavelengths, especially when small tissue geometries and high light absorption are encountered. The SP_N equations have already been applied for solving neutron transport problems in nuclear sciences, but until now have not been used for solving problems in tissue optics. For the first time, we have derived the SP_N equations up to order $N = 7$ for anisotropically scattering media and partially reflective boundary conditions, and we provide solutions for the exiting partial current.

Light propagation models in biomedical optics are essential for tomographic imaging of biological tissue using visible and near-infrared light [1]. These models predict light intensities, which are subsequently compared to measured light intensities on the tissue boundary. Based on the predicted and measured data, image reconstruction algorithms recover either the spatial distributions of intrinsic optical tissue properties or the concentrations of light emitting molecular probes inside tissue. For example, diffuse optical tomography (DOT) of tissue parameters has been employed in breast imaging for breast cancer diagnosis [1], in functional brain imaging of blood oxygenation [2], in imaging of small joints for early diagnosis of rheumatoid arthritis [3], and in small animal imaging for studying physiological processes and pathologies [4]. Tomographic imaging of fluorescent and bioluminescent light sources inside tissue is used in fluorescence molecular tomography (FMT) and bioluminescence tomography (BLT) [5]. The targets of these imaging modalities are exogenous fluorescent reporter probes, endogenous fluorescent reporter proteins, and bioluminescent enzymes in small animal models of human disease. Tomographic imaging of light emitting sources is a valuable tool for drug development and for studying cellular and molecular processes in vivo. The development of new light propagation models, which are computationally more efficient and provide solutions with higher accuracy, will facilitate and improve the outcome of optical image reconstruction calculations. Most light propagation models are based or derived from the ERT. But, which particular light propagation model is used depends on the optical wavelength of the light and the spatial size of the tissue domain interacting with the light.

The light-tissue interaction is governed by the optical tissue parameters, such as the *scattering*, μ_s, and the *absorption*, μ_a, coefficients, which are wavelength-dependent. The absorption coefficient, which can vary over several orders of magnitude, increases towards the visible wavelengths. Typical absorption parameters are in the range of 0.5–5 cm^{-1} at wavelengths $\lambda < 625$ nm. In the red and near-infrared regions with $\lambda > 625$ nm, the absorption coefficient varies between 0.01 and 0.5 cm^{-1}. On the other hand, the scattering coefficient varies only slightly as a function of the wavelength between 10 and 200 cm^{-1}. Light scattering events are strongly forward-peaked and are well-described by the Henyey–Greenstein scattering kernel with the *mean scattering cosine* (also termed *anisotropy factor*) g, which varies typically between 0.5 and 0.95 depending on the tissue type. The *reduced scattering coefficient* is defined as $\mu_s' = (1 - g)\mu_s$. Typical reduced scattering coefficients are between 4 and 15 cm^{-1} and are slightly wavelength-dependent. The *mean free path* (mfp) is the length $1/(\mu_s + \mu_a)$, whereas the *transport mean free path* (tmfp) is defined as the length $1/(\mu_s' + \mu_a)$, which plays an important role in diffusion theory. We refer the reader to [6–8] for a comprehensive review of optical tissue parameters.

Most light propagation models in optical tomography are based on the diffusion approximation to the ERT when the condition $\mu_a \ll \mu_s'$ holds. The diffusion model is widely applied in DOT to tissues with relatively large geometries, such as human brain and breast tissue [1]. However, when imaging small tissue geometries, e.g. whole-body imaging of small animals [4], the diffusion model becomes less attractive, partly because boundary effects are significant due to the increased tissue boundary to tissue volume ratio. Another important fact of the limited validity of the diffusion model in whole-body small animal imaging is the large range of the absorption coefficients for different interior organs and tissue types when probing with near-infrared light. The absorption coefficient of most tissue types is $\mu_a \ll \mu_s'$ for $\lambda > 700$ nm, and here the diffusion model is valid.

However, this is not the case for highly vascularized tissues, due to the increased light absorption of hemoglobin. Typical absorption coefficients at $650 < \lambda < 900$ nm for liver, kidneys, heart, and aorta of small animals (mice, rats) are between 0.7 and 2.7 cm^{-1} [6–8]. Hence, the diffusion model has limited validity when modeling light propagation in the vicinity of those highly vascularized tissue parts [9,10].

When using visible instead of near-infrared light, as is done in FMT of green (GFP), yellow (YFP), and red (DsRed) fluorescent proteins or of bioluminescent luciferase in BLT [11,12], large absorption coefficients are encountered. For example, the emission peaks of GFP and DsRed are at 510 and 570 nm, whereas their excitation peaks are at 488 and 555 nm. Different firefly luciferases have emission peaks at 538–570 nm [12–14]. Hence, fluorescent and bioluminescent light, propagating to the tissue surface, is strongly absorbed by hemoglobin and other tissue chromophores. The large absorption coefficients at those wavelengths make the diffusion model as a light propagation model less accurate [9,10]. Tomographic imaging, which relies on an accurate light propagation model, will subsequently lead to erroneous reconstruction results of the sought fluorescent and bioluminescent source distributions.

Higher-order approximations to the ERT are required, such as the discrete-ordinates (S_N) [15,16] or spherical harmonics (P_N) [15,17,18] approximations, to overcome the limiting constraints of using the diffusion model. Both methods have already been implemented and applied in tissue optics, with promising results [10,19]. The S_N and P_N approximations yield exact transport solutions as $N \to \infty$. The number of P_N equations grows as $(N + 1)^2$ for a three-dimensional (3-D) medium. The S_N method uses discrete ordinates and solves a system of $N(N + 2)$ coupled equations. Consequently, the S_N and P_N methods are computationally expensive, and, e.g., a full 3-D image reconstruction of a mouse model for recovering the fluorescent probe distribution can take up several hours or days of computation time [19]. Also, the S_N method suffers from an increased ray effect in the vicinity of sources when highly absorbing media are present [1,10].

Therefore, we have developed a light propagation model that is based on the simplified spherical harmonics or SP_N approximation to the ERT. The SP_N method was originally proposed by Gelbard [20,21] for neutron transport, but a thorough theoretical foundation was laid out by Larsen and co-workers only during the 1990's [22–26]. The SP_N equations have also been applied to other problems in particle transport and heat radiation transfer [27–33]. However, there are distinct differences between the formulations of the SP_N equations in nuclear sciences and tissues optics. SP_N applications in the nuclear engineering community have focused on problems that are driven by internal sources, with no radiation entering the system through its outer boundaries. Applications in tissue optics constitute the opposite regime, where the light propagation is usually driven by external sources on the tissue surface. Also, the boundary conditions in tissue optics have nonlinear partial reflection, in which some of the exiting photons are reflected back into the system, but partial reflection is absent in nuclear radiation problems. Furthermore, nuclear radiation problems focus on obtaining estimates of the fluence at spatial points within the physical system, whereas photonic problems in biological tissue require accurate estimates of the exiting partial current on the outer boundary of the system. And last, the applications of SP_N methods for neutrons and high-energy photons in nuclear sciences have dealt mainly with isotropic and weakly-anisotropic scattering, but SP_N methods in tissue optics need to take the more highly anisotropic scattering of photons into account. (However, we note that Josef and Morel have successfully applied the SP_N approximation to 2-D electron–photon problems, and that electron transport is much more severely forward-peaked, with much smaller mean free paths, than photon transport in tissue [30]. This strongly suggests that the SP_N approximation will be adequate for the anisotropic scattering in tissue optics.)

The SP_N equations have several advantages when compared to the S_N and full P_N equations. First, the SP_N method approximates the ERT by a set of coupled diffusion-like equations with *Laplacian* operators. Thus, the SP_N method avoids the complexities of the full P_N approximation, in which mixed spatial derivatives instead of Laplacians occur. Second, the SP_N approximation captures most of the transport corrections to the diffusion approximation [23]. Third, there are fewer equations to solve than with the full P_N or S_N method. Fourth, the SP_N system can be solved with standard diffusion solvers, and the solution can be obtained several orders of magnitude faster than with the S_N or P_N methods. Last, the SP_N method does not suffer from ray effects, as the S_N method does. A disadvantage of the SP_N methods has historically been its weak theoretical foundation [25], and its full appreciation in nuclear radiological sciences was only gained within the last decade. Furthermore, SP_N solutions do not converge to exact transport solutions as $N \to \infty$. Instead, the SP_N

solution is asymptotic; for each problem, there is an optimal N that yields the best solution. Only for one-dimensional (1-D) problems are the SP_N and P_N equations and boundary conditions the same, yielding identical solutions.

Until now, the SP_N approximation has not been formulated for physical problems in tissue optics. Our goal in this paper is to fully establish a comprehensive mathematical framework of SP_N equations for solving the physically relevant light propagation problems in biological tissue. Specifically, (i) we formulate the SP_N equations up to order $N = 7$ for partially reflective boundary conditions and anisotropically scattering media. The derived system of SP_N equations results either in the diffusion, SP_3, SP_5, or SP_7 approximations. Partially reflective boundary conditions are taken into account by providing the refractive index of the tissue. Anisotropic light scattering in tissue is addressed by including the Henyey–Greenstein phase function into the SP_N framework. (ii) We numerically solve the SP_N equations for two-dimensional media with typical tissue properties at visible and near-infrared wavelengths, and compare the numerical results to solutions obtained from the discrete-ordinates method. Since we expect an asymptotic behavior of the SP_N solutions with increasing N, we will determine an N that gives best solutions. Finally, (iii) we show that the SP_N equations provide solutions that are significantly more accurate than diffusion solutions. We demonstrate that SP_N equations provide accurate solutions for media with transportive properties, significant for small animal imaging at visible and near-infrared wavelengths, but at a much lower computational cost than solving the discrete-ordinates transport equations.

The remainder of this paper is organized as follows. In Section 2 we introduce the underlying ERT for light propagation in tissue. In Section 3 we derive the SP_N equations for anisotropically scattering media and with partially reflective boundary conditions. A benchmark based on an S_N method is provided in Section 4, which will subsequently be used for a numerical validation of the SP_N method in Section 5. A discussion and conclusion will be given in the last section.

2. Equation of radiative transfer

The ERT defines the *radiance* $\psi(\boldsymbol{r}, \boldsymbol{\Omega})$, with units of W cm^{-2} sr^{-1}, at the spatial point $\boldsymbol{r} \in V$ and direction-of-flight (unit vector) $\boldsymbol{\Omega}$:

$$\boldsymbol{\Omega} \cdot \nabla \psi(\boldsymbol{r}, \boldsymbol{\Omega}) + \mu_t(\boldsymbol{r}) \psi(\boldsymbol{r}, \boldsymbol{\Omega}) = \mu_s(\boldsymbol{r}) \int_{4\pi} p(\boldsymbol{\Omega} \cdot \boldsymbol{\Omega}') \psi(\boldsymbol{r}, \boldsymbol{\Omega}') \, \mathrm{d}\Omega' + \frac{Q(\boldsymbol{r})}{4\pi}. \tag{1}$$

The *attenuation coefficient* μ_t, with units of cm^{-1}, is the sum of the absorption μ_a and scattering μ_s coefficients. The *phase function* $p(\boldsymbol{\Omega} \cdot \boldsymbol{\Omega}')$ is the distribution function for photons anisotropically scattering from direction $\boldsymbol{\Omega}'$ to direction $\boldsymbol{\Omega}$. $Q(\boldsymbol{r})$ describes an isotropic interior photon source density. The *fluence* ϕ in units of W cm^{-2} is defined by:

$$\phi(\boldsymbol{r}) = \int_{4\pi} \psi(\boldsymbol{r}, \boldsymbol{\Omega}) \, \mathrm{d}\Omega. \tag{2}$$

2.1. Boundary conditions and detector readings

Photons that propagate from boundary points $\boldsymbol{r} \in \partial V$ into V originate from (i) an external boundary source $S(\boldsymbol{r}, \boldsymbol{\Omega})$, and (ii) photons that attempt to leak out through ∂V, but due to the refractive index mismatch at ∂V, are reflected specularly back into V with probability R. The *partly-reflecting boundary condition* specifies ψ as the sum of these two contributions:

$$\psi(\boldsymbol{r}, \boldsymbol{\Omega}) = S(\boldsymbol{r}, \boldsymbol{\Omega}) + R(\boldsymbol{\Omega}' \cdot \boldsymbol{n}) \psi(\boldsymbol{r}, \boldsymbol{\Omega}'), \quad \boldsymbol{r} \in \partial V, \ \boldsymbol{\Omega} \cdot \boldsymbol{n} < 0. \tag{3}$$

Here $\boldsymbol{n}$ is the unit outer normal vector and $\boldsymbol{\Omega}$ is the specular reflection of $\boldsymbol{\Omega}'$, which points outward (satisfies $\boldsymbol{\Omega}' \cdot \boldsymbol{n} > 0$):

$$\boldsymbol{\Omega}' = \boldsymbol{\Omega} - 2(\boldsymbol{\Omega} \cdot \boldsymbol{n})\boldsymbol{n}. \tag{4}$$

The *reflectivity* $R(\cos \vartheta')$ in Eq. (3) is given by:

$$R(\cos \vartheta') = \begin{cases} \frac{1}{2}\left(\frac{n_m \cos \vartheta'' - n_0 \cos \vartheta'}{n_m \cos \vartheta'' + n_0 \cos \vartheta'}\right)^2 + \frac{1}{2}\left(\frac{n_m \cos \vartheta' - n_0 \cos \vartheta''}{n_m \cos \vartheta' + n_0 \cos \vartheta''}\right)^2, & \vartheta' < \vartheta_c, \\ 1, & \vartheta' \geqslant \vartheta_c, \end{cases} \tag{5}$$

where the angle ϑ' from within the medium with refractive index n_m satisfies $\cos \vartheta' = \mathbf{\Omega}' \cdot \mathbf{n}$, and the refracted angle ϑ'' in the outside medium (air) with $n_0 = 1$ satisfies *Snell's law*: $n_m \sin \vartheta' = n_0 \sin \vartheta''$. The critical angle ϑ_c' for total internal reflection ($R = 1$) is given by $n_m \sin \vartheta_c' = n_0$. The term $S(\mathbf{r}, \mathbf{\Omega})$, having the same units as ψ, describes an external photon source at the tissue boundary.

The detector readings are obtained from the exiting partial current $J^+(\mathbf{r})$ at ∂V. At each point $\mathbf{r} \in \partial V$ for which the external source $S(\mathbf{r}, \mathbf{\Omega}) = 0$, we have:

$$J^+(\mathbf{r}) = \int_{\mathbf{\Omega} \cdot \mathbf{n} > 0} [1 - R(\mathbf{\Omega} \cdot \mathbf{n})](\mathbf{\Omega} \cdot \mathbf{n})\psi(\mathbf{r}, \mathbf{\Omega}) \, d\Omega. \tag{6}$$

2.2. Phase function

The phase function $p(\mathbf{\Omega} \cdot \mathbf{\Omega}')$, with units of sr^{-1}, has the following interpretation: $p(\mathbf{\Omega} \cdot \mathbf{\Omega}') \, d\Omega =$ the probability that when a photon traveling in direction $\mathbf{\Omega}'$ scatters, the scattered direction of flight will occur in $d\Omega$ about $\mathbf{\Omega}$. The angle ϑ between the incident direction of flight $\mathbf{\Omega}'$ and the exiting direction of flight $\mathbf{\Omega}$ is the *scattering angle*, and $\cos \vartheta = \mathbf{\Omega}' \cdot \mathbf{\Omega}$. Biological tissue is anisotropically-scattering, with a highly forward-peaked phase function. A commonly-applied phase function in tissue optics is the Henyey–Greenstein phase function [34,35]:

$$p(\cos \theta) = \frac{1 - g^2}{4\pi(1 + g^2 - 2g \cos \theta)^{3/2}}. \tag{7a}$$

This model is widely-used because (i) it is accurate, (ii) it depends on a single adjustable parameter g, which can be space-dependent, and (iii) it has the following simple Legendre polynomial expansion:

$$p(\cos \theta) = \sum_{n=0}^{\infty} \frac{2n + 1}{4\pi} g^n P_n(\cos \theta). \tag{7b}$$

Now we define the *differential scattering coefficient* $\mu_s(\mathbf{r}, \cos \theta) = \mu_s(\mathbf{r})p(\cos \theta)$ and write the equation of radiative transfer as:

$$\mathbf{\Omega} \cdot \nabla \psi(\mathbf{r}, \mathbf{\Omega}) + \mu_t(\mathbf{r})\psi(\mathbf{r}, \mathbf{\Omega}) = \int_{4\pi} \mu_s(\mathbf{r}, \mathbf{\Omega} \cdot \mathbf{\Omega}')\psi(\mathbf{r}, \mathbf{\Omega}') \, d\Omega' + \frac{Q(\mathbf{r})}{4\pi}. \tag{8}$$

3. SP_N methods

The SP_N equations have been derived in three ways: (i) by a formal procedure, in which they are hypothesized as multi-dimensional generalizations of the 1-D P_N equations, (ii) by an asymptotic analysis, in which they are shown to be asymptotic corrections to diffusion theory, and (iii) by a variational analysis. The first (formal) approach was historically the first to be proposed, in the early 1960's [20]. This approach is relatively simple, but is theoretically weak. The second (asymptotic) approach was developed in the 1990's [23]; this is much more theoretically convincing, but it only leads to the basic SP_N equations without boundary conditions (the boundary conditions must be hypothesized). The third (variational) approach was also developed in the 1990's [22,25]; this yields both the SP_N equations and their boundary conditions. Unfortunately, from the algebraic viewpoint, the variational derivation is exceedingly complicated.

In the subsequent sections of this paper, we present the formal derivation of the SP_7 equations for the case of fully anisotropic scattering, with the partly-reflecting boundary conditions of Eq. (3). These new results have not previously been published. The simpler SP_5, SP_3, and $SP_1 =$ diffusion approximations are easily obtained from the results presented here.

3.1. The planar-geometry P_N method

To begin, we formulate the planar-geometry version of Eq. (1) with the partially-reflective boundary condition (3). We consider the planar system $0 \leqslant x \leqslant X$; the corresponding planar-geometry version of Eq. (1) is:

$$\omega \frac{\partial \psi}{\partial x}(x, \omega) + \mu_t(x)\psi(x, \omega) = \int_{-1}^{1} \mu_s(x, \omega, \omega')\psi(x, \omega')\, d\omega' + \frac{Q(x)}{2}, \tag{9}$$

with:

$$\mu_s(x, \omega, \omega') = \sum_{n=0}^{\infty} \frac{2n+1}{2}\mu_s(x)g^n P_n(\omega)P_n(\omega'). \tag{10}$$

The partly-reflecting boundary conditions are:

$$\psi(0, \omega) = S(0, \omega) + R(\omega)\psi(0, -\omega), \quad 0 < \omega \leqslant 1, \tag{11a}$$

$$\psi(X, \omega) = S(X, \omega) + R(-\omega)\psi(X, -\omega), \quad -1 \leqslant \omega < 0. \tag{11b}$$

Next, we calculate the P_N approximation to this 1-D problem. For $n \geqslant 0$, we define the *Legendre moments* of the radiance:

$$\phi_n(x) = \int_{-1}^{1} P_n(\omega)\psi(x, \omega)\, d\omega, \tag{12}$$

and the nth-*order absorption coefficients*:

$$\mu_{an}(x) = \mu_t(x) - \mu_s(x)g^n. \tag{13}$$

(Note that for $n = 0$: $\mu_{a0} = \mu_t - \mu_s = \mu_a$; and for $n = 1$: $\mu_{a1} = \mu_t - \mu_s g = \mu_s' + \mu_a$.) Then, for $n \geqslant 0$, we operate on Eq. (9) by $\int_{-1}^{1} P_n(\omega)(\cdot)\, d\omega$ to obtain:

$$\frac{n+1}{2n+1} \frac{d\phi_{n+1}}{dx}(x) + \frac{n}{2n+1} \frac{d\phi_{n-1}}{dx}(x) + \mu_{an}(x)\phi_n(x) = \delta_{n0}Q(x), \tag{14}$$

with $\phi_{-1} = 0$. Also, for $n \geqslant 1$ and odd, we operate on Eq. (11b) by $\int_{-1}^{0} P_n(\omega)(\cdot)\, d\omega$ to obtain:

$$\int_{-1}^{0} P_n(\omega)\psi(X, \omega)\, d\omega = \int_{-1}^{0} P_n(\omega)S(X, \omega)\, d\omega + \int_{-1}^{0} P_n(\omega)R(-\omega)\psi(X, -\omega)\, d\omega. \tag{15}$$

[A similar equation can be derived from Eq. (11a), but we will not do this here.] Eq. (14) for $n \geqslant 0$ and (15) for $n \geqslant 1$ and n odd are exact, but they do not yield a closed system of equations for a finite number of the Legendre moments ϕ_n.

To close this system by the P_N approximation, we select an odd positive integer N and take [36]:

$$\psi(x, \omega) \approx \sum_{n=0}^{N} \frac{2n+1}{2}\phi_n(x)P_n(\omega). \tag{16a}$$

This approximation is equivalent to setting:

$$\phi_n(x) = 0, \quad N < n < \infty. \tag{16b}$$

Then, (i) we introduce Eq. (16b) into Eq. (14) and require that result to hold for $0 \leqslant n \leqslant N$; and (ii) we introduce Eq. (16a) into Eq. (15) and require that result to hold for $1 \leqslant n \leqslant N$ and N odd. For the $N+1$ unknown functions $\phi_n(x)$, $0 \leqslant n \leqslant N$, this yields a closed system of (i) $N+1$ first-order differential equations in $0 \leqslant x \leqslant X$, and (ii) $(N+1)/2$ boundary conditions at each boundary point.

To proceed, we rewrite this system by algebraically eliminating the odd-order moments. For $1 \leqslant n \leqslant N$ and n odd, Eq. (14) gives:

$$\phi_n(x) = -\frac{1}{\mu_{an}(x)} \frac{d}{dx}\left[\frac{n+1}{2n+1}\phi_{n+1}(x) + \frac{n}{2n+1}\phi_{n-1}(x)\right]. \tag{17}$$

Using this result to eliminate the odd-order moments in the remaining of Eq. (14), we obtain the following second-order equations for the even-order moments:

$$
-\left(\frac{n+1}{2n+1}\right)\frac{\mathrm{d}}{\mathrm{d}x}\frac{1}{\mu_{a,n+1}}\frac{\mathrm{d}}{\mathrm{d}x}\left[\left(\frac{n+2}{2n+3}\right)\phi_{n+2}+\left(\frac{n+1}{2n+3}\right)\phi_{n}\right]
$$
$$
-\left(\frac{n}{2n+1}\right)\frac{\mathrm{d}}{\mathrm{d}x}\frac{1}{\mu_{a,n-1}}\frac{\mathrm{d}}{\mathrm{d}x}\left[\left(\frac{n}{2n-1}\right)\phi_{n}+\left(\frac{n-1}{2n-1}\right)\phi_{n-2}\right]+\mu_{an}\phi_{n}=Q.
\tag{18}
$$

These equations hold for $0 \leqslant n \leqslant N-1$ and n even; and with $0 = \phi_{-2} = \phi_{N+1}$.

Also, we use Eq. (17) to eliminate the odd-order moments in Eq. (16a), and then in the boundary condition (15). The end result is a system of $(N+1)/2$ second-order differential equations defined on $0 \leqslant x \leqslant X$ (Eq. (18)), with $(N+1)/2$ boundary conditions imposed at each of the two boundary points $x = 0, X$, for the $(N+1)/2$ even-order moments $\phi_0, \phi_2, \ldots, \phi_{N-1}$.

The differential equations obtained by this process (Eq. (18)) involve conventional second-order diffusion operators. The boundary conditions are *mixed*; they consist of linear combinations of the even-order ϕ_n and their first x-derivatives. This well-defined system of equations constitutes the *second-order form of the P_N approximation* to the planar-geometry transport problem of Eqs. (9)–(11).

P_N approximations can also be derived for multidimensional problems. However, to do this, it is necessary to expand the angular variable in terms of the spherical harmonic functions, which depend on two scalar angles, not one. This greatly increases the complexity of the multi-D P_N approximation; for a given odd order N one obtains many extra unknowns and equations than in 1-D. Also, the equations no longer have the relatively simple diffusion character of Eq. (18). For these reasons, the multidimensional P_N equations are not widely used. However, the Simplified P_N or SP_N equations, discussed next, have found increasing applications in recent years.

3.2. The SP_N equations

In the formal derivation of the 3-D SP_N equations, one simply takes the 1-D P_N equations and replaces each 1-D diffusion operator by its 3-D counterpart. That is, we replace:

$$
\frac{\mathrm{d}}{\mathrm{d}x}\frac{1}{\mu_{an}(x)}\frac{\mathrm{d}}{\mathrm{d}x}\phi(x) \quad \text{by} \quad \nabla\cdot\frac{1}{\mu_{an}(\boldsymbol{r})}\nabla\phi(\boldsymbol{r}).
\tag{19}
$$

Thus, Eq. (18) become:

$$
-\left(\frac{n+1}{2n+1}\right)\nabla\cdot\frac{1}{\mu_{a,n+1}}\nabla\left[\left(\frac{n+2}{2n+3}\right)\phi_{n+2}+\left(\frac{n+1}{2n+3}\right)\phi_{n}\right]
$$
$$
-\left(\frac{n}{2n+1}\right)\nabla\cdot\frac{1}{\mu_{a,n-1}}\nabla\left[\left(\frac{n}{2n-1}\right)\phi_{n}+\left(\frac{n-1}{2n-1}\right)\phi_{n-2}\right]+\mu_{an}\phi_{n}=Q.
\tag{20}
$$

For the case $N = 7$, it is useful to rewrite these equations in terms of the *composite moments*:

$$
\begin{aligned}
\varphi_1 &= \phi_0 + 2\phi_2,\\
\varphi_2 &= 3\phi_2 + 4\phi_4,\\
\varphi_3 &= 5\phi_4 + 6\phi_6,\\
\varphi_4 &= 7\phi_6.
\end{aligned}
\tag{21}
$$

These imply:

$$
\phi_6 = \frac{1}{7}\varphi_4,
\tag{22a}
$$

$$
\phi_4 = \frac{1}{5}\varphi_3 - \frac{6}{35}\varphi_4,
\tag{22b}
$$

$$\phi_2 = \frac{1}{3}\varphi_2 - \frac{4}{15}\varphi_3 + \frac{8}{35}\varphi_4, \tag{22c}$$

$$\phi_0 = \varphi_1 - \frac{2}{3}\varphi_2 + \frac{8}{15}\varphi_3 - \frac{16}{35}\varphi_4. \tag{22d}$$

Then Eqs. (20) can be rearranged into the following four coupled diffusion equations for the four composite moments:

$$-\nabla \cdot \frac{1}{3\mu_{a1}}\nabla\varphi_1 + \mu_a\varphi_1 = Q + \left(\frac{2}{3}\mu_a\right)\varphi_2 - \left(\frac{8}{15}\mu_a\right)\varphi_3 + \left(\frac{16}{35}\mu_a\right)\varphi_4, \tag{23a}$$

$$-\nabla \cdot \frac{1}{7\mu_{a3}}\nabla\varphi_2 + \left(\frac{4}{9}\mu_a + \frac{5}{9}\mu_{a2}\right)\varphi_2 = -\frac{2}{3}Q + \left(\frac{2}{3}\mu_a\right)\varphi_1 + \left(\frac{16}{45}\mu_a + \frac{4}{9}\mu_{a2}\right)\varphi_3 - \left(\frac{32}{105}\mu_a + \frac{8}{21}\mu_{a2}\right)\varphi_4, \tag{23b}$$

$$-\nabla \cdot \frac{1}{11\mu_{a5}}\nabla\varphi_3 + \left(\frac{64}{225}\mu_a + \frac{16}{45}\mu_{a2} + \frac{9}{25}\mu_{a4}\right)\varphi_3 = \frac{8}{15}Q - \left(\frac{8}{15}\mu_a\right)\varphi_1 + \left(\frac{16}{45}\mu_a + \frac{4}{9}\mu_{a2}\right)\varphi_2$$
$$+ \left(\frac{128}{525}\mu_a + \frac{32}{105}\mu_{a2} + \frac{54}{175}\mu_{a4}\right)\varphi_4, \tag{23c}$$

$$-\nabla \cdot \frac{1}{15\mu_{a7}}\nabla\varphi_4 + \left(\frac{256}{1225}\mu_a + \frac{64}{245}\mu_{a2} + \frac{324}{1225}\mu_{a4} + \frac{13}{49}\mu_{a6}\right)\varphi_4 = -\frac{16}{35}Q + \left(\frac{16}{35}\mu_a\right)\varphi_1$$
$$- \left(\frac{32}{105}\mu_a + \frac{8}{21}\mu_{a2}\right)\varphi_2 + \left(\frac{128}{525}\mu_a + \frac{32}{105}\mu_{a2} + \frac{54}{175}\mu_{a4}\right)\varphi_3. \tag{23d}$$

These are the 3-D SP_7 equations.

The SP_5 equations are obtained by setting $\phi_6 = 0$ and solving Eqs. (23a)–(23c) for φ_1, φ_2, and φ_3. The SP_3 equations are obtained by setting $\phi_6 = \phi_4 = 0$ and solving Eqs. (23a), (23b) for φ_1 and φ_2. The SP_1 (diffusion) equation is obtained by setting $\phi_6 = \phi_4 = \phi_2 = 0$ and solving Eq. (23a) for φ_1. [In all cases, the scalar flux is obtained from Eq. (22d).] Thus, we explicitly have the SP_1 (diffusion) equation:

$$-\nabla \cdot \frac{1}{3\mu_{a1}(\boldsymbol{r})}\nabla\phi_0(\boldsymbol{r}) + \mu_a(\boldsymbol{r})\phi_0(\boldsymbol{r}) = Q(\boldsymbol{r}). \tag{24}$$

3.3. The SP_N boundary conditions

As described previously, the 1-D P_7 boundary conditions at $x = X$ are obtained by (i) using Eq. (17) to eliminate the odd-order moments in Eq. (16a) with $N = 7$, (ii) introducing this approximation into Eq. (15) with $n = 1, 3, 5$, and 7; and (iii) using Eqs. (22) to cast these results into equations for the composite moments. This results in four equations, each consisting of a linear combination of the composite moments and their first derivatives with respect to x.

In the formal derivation of the 3-D SP_N boundary conditions, we take the mixed 1-D P_N boundary condition at $x = X$ and interpret the spatial derivative $d\varphi/dx$ as the directional derivative of φ in the direction of the outward normal vector $\boldsymbol{n}$. Thus, we take the 1-D boundary condition at $x = X$ and replace

$$\frac{d\varphi}{dx}(X) \quad \text{by } \boldsymbol{n} \cdot \nabla\varphi(\boldsymbol{r}). \tag{25}$$

In the formulation of these boundary conditions, various angular moments of the reflectivity R occur. We define these as:

$$R_n = \int_0^1 R(\omega)\omega^n \, d\omega. \tag{26}$$

These constants depend on the refractive indices and must be pre-calculated. Also, we replace angular integrals (over the incoming directions) of the external source

$$\int_{-1}^{0} |\omega|^m S(X,\omega)\, d\omega \quad \text{by} \quad \int_{\boldsymbol{\Omega}\cdot\boldsymbol{n}<0} |\boldsymbol{\Omega}\cdot\boldsymbol{n}|^m S(\boldsymbol{r},\boldsymbol{\Omega})\, d\Omega. \tag{27}$$

We will not include in this paper the straightforward but lengthy algebra required to derive these equations; instead, we will just state the final results:

$$\left(\frac{1}{2}+A_1\right)\varphi_1 + \left(\frac{1+B_1}{3\mu_{a1}}\right)\boldsymbol{n}\cdot\nabla\varphi_1 = \left(\frac{1}{8}+C_1\right)\varphi_2 + \left(\frac{D_1}{\mu_{a3}}\right)\boldsymbol{n}\cdot\nabla\varphi_2 + \left(-\frac{1}{16}+E_1\right)\varphi_3 + \left(\frac{F_1}{\mu_{a5}}\right)\boldsymbol{n}\cdot\nabla\varphi_3$$
$$+ \left(\frac{5}{128}+G_1\right)\varphi_4 + \left(\frac{H_1}{\mu_{a7}}\right)\boldsymbol{n}\cdot\nabla\varphi_4 + \int_{\boldsymbol{\Omega}\cdot\boldsymbol{n}<0} S(\boldsymbol{\Omega})2|\boldsymbol{\Omega}\cdot\boldsymbol{n}|\, d\Omega, \tag{28a}$$

$$\left(\frac{7}{24}+A_2\right)\varphi_2 + \left(\frac{1+B_2}{7\mu_{a3}}\right)\boldsymbol{n}\cdot\nabla\varphi_2 = \left(\frac{1}{8}+C_2\right)\varphi_1 + \left(\frac{D_2}{\mu_{a1}}\right)\boldsymbol{n}\cdot\nabla\varphi_1 + \left(\frac{41}{384}+E_2\right)\varphi_3 + \left(\frac{F_2}{\mu_{a5}}\right)\boldsymbol{n}\cdot\nabla\varphi_3$$
$$+ \left(-\frac{1}{16}+G_2\right)\varphi_4 + \left(\frac{H_2}{\mu_{a7}}\right)\boldsymbol{n}\cdot\nabla\varphi_4 + \int_{\boldsymbol{\Omega}\cdot\boldsymbol{n}<0} S(\boldsymbol{\Omega})(5|\boldsymbol{\Omega}\cdot\boldsymbol{n}|^3 - 3|\boldsymbol{\Omega}\cdot\boldsymbol{n}|)\, d\Omega, \tag{28b}$$

$$\left(\frac{407}{1920}+A_3\right)\varphi_3 + \left(\frac{1+B_3}{11\mu_{a5}}\right)\boldsymbol{n}\cdot\nabla\varphi_3 = \left(-\frac{1}{16}+C_3\right)\varphi_1 + \left(\frac{D_3}{\mu_{a1}}\right)\boldsymbol{n}\cdot\nabla\varphi_1 + \left(\frac{41}{384}+E_3\right)\varphi_2 + \left(\frac{F_3}{\mu_{a3}}\right)\boldsymbol{n}\cdot\nabla\varphi_2$$
$$+ \left(\frac{233}{2560}+G_3\right)\varphi_4 + \left(\frac{H_3}{\mu_{a7}}\right)\boldsymbol{n}\cdot\nabla\varphi_4$$
$$+ \int_{\boldsymbol{\Omega}\cdot\boldsymbol{n}<0} S(\boldsymbol{\Omega})\left(\frac{63}{4}|\boldsymbol{\Omega}\cdot\boldsymbol{n}|^5 - \frac{35}{2}|\boldsymbol{\Omega}\cdot\boldsymbol{n}|^3 + \frac{15}{4}|\boldsymbol{\Omega}\cdot\boldsymbol{n}|\right)\, d\Omega, \tag{28c}$$

$$\left(\frac{3023}{17920}+A_4\right)\varphi_4 + \left(\frac{1+B_4}{15\mu_{a7}}\right)\boldsymbol{n}\cdot\nabla\varphi_4 = \left(\frac{5}{128}+C_4\right)\varphi_1 + \left(\frac{D_4}{\mu_{a1}}\right)\boldsymbol{n}\cdot\nabla\varphi_1 + \left(-\frac{1}{16}+E_4\right)\varphi_2$$
$$+ \left(\frac{F_4}{\mu_{a3}}\right)\boldsymbol{n}\cdot\nabla\varphi_2 + \left(\frac{233}{2560}+G_4\right)\varphi_3 + \left(\frac{H_4}{\mu_{a5}}\right)\boldsymbol{n}\cdot\nabla\varphi_3$$
$$+ \int_{\boldsymbol{\Omega}\cdot\boldsymbol{n}<0} S(\boldsymbol{\Omega})\left(\frac{429}{8}|\boldsymbol{\Omega}\cdot\boldsymbol{n}|^7 - \frac{693}{8}|\boldsymbol{\Omega}\cdot\boldsymbol{n}|^5 + \frac{315}{8}|\boldsymbol{\Omega}\cdot\boldsymbol{n}|^3 - \frac{35}{8}|\boldsymbol{\Omega}\cdot\boldsymbol{n}|\right)\, d\Omega. \tag{28d}$$

The coefficients $A_1,\ldots,H_1,\ldots,A_4,\ldots,H_4$ in these equations are defined in Appendix (A.1)–(A.5).

The SP_5 boundary conditions are given by Eqs. (28a)–(28c) with $\phi_6 = 0$. The SP_3 boundary conditions are given by Eqs. (28a) and (28b) with $\phi_6 = \phi_4 = 0$. The diffusion boundary condition is given by Eq. (28a) with $\phi_6 = \phi_4 = \phi_2 = 0$. Thus, we obtain the following 3-D diffusion boundary condition [37–39]:

$$\left(\frac{1}{2}+A_1\right)\phi_0 + \left(\frac{1+B_1}{3\mu_{a1}}\right)\boldsymbol{n}\cdot\nabla\phi_0 = \int_{\boldsymbol{\Omega}\cdot\boldsymbol{n}<0} S(\boldsymbol{\Omega})2|\boldsymbol{\Omega}\cdot\boldsymbol{n}|\, d\Omega. \tag{29}$$

3.4. Detector readings

The detector readings are obtained from the exiting partial current J^+ at the tissue boundary ∂V. At the right boundary point $x = X$ in the 1-D planar medium, assuming that the external source $S(X,\omega) = 0$ at this point, we have:

$$J^+(X) = \int_0^1 [1 - R(\omega)]\omega\psi(x,\omega)\, d\omega. \tag{30}$$

Substituting the approximation (16a) with $N = 7$ into Eq. (30), we obtain the exiting partial current $J^+(X)$ as a function of the Legendre moments $\phi_n(X)$:

$$J^+ = \left(\frac{1}{4} + J_0\right)\phi_0 + \left(\frac{1}{2} + J_1\right)\phi_1 + \left(\frac{5}{16} + J_2\right)\phi_2 + J_3\phi_3 + \left(-\frac{3}{32} + J_4\right)\phi_4 + J_5\phi_5 + \left(\frac{13}{256} + J_6\right)\phi_6 + J_7\phi_7,$$

(31)

where the coefficients J_n are given in the Appendix (Eqs. (A.6)). Using Eq. (17), we eliminate the odd-order moments to obtain the exiting partial current in terms of the even-order moments:

$$J^+ = \left(\frac{1}{4} + J_0\right)\phi_0 - \left(\frac{0.5 + J_1}{3\mu_{a1}}\right)\frac{\mathrm{d}}{\mathrm{d}x}(\phi_0 + 2\phi_2) + \left(\frac{5}{16} + J_2\right)\phi_2 - \left(\frac{J_3}{7\mu_{a3}}\right)\frac{\mathrm{d}}{\mathrm{d}x}(3\phi_2 + 4\phi_4)$$
$$+ \left(-\frac{3}{32} + J_4\right)\phi_4 - \left(\frac{J_5}{11\mu_{a5}}\right)\frac{\mathrm{d}}{\mathrm{d}x}(5\phi_4 + 6\phi_6) + \left(\frac{13}{256} + J_6\right)\phi_6 - \left(\frac{J_7}{15\mu_{a7}}\right)\frac{\mathrm{d}}{\mathrm{d}x}(7\phi_6).$$

Finally, we introduce into this equation the composite moments (Eqs. (21) and (22)); and for a 3-D problem we replace $\mathrm{d}/\mathrm{d}x$ by the outward normal derivative $\boldsymbol{n} \cdot \nabla$. We obtain the following SP_7 expression for the exiting partial current $J^+(\boldsymbol{r})$, for each point $\boldsymbol{r} \in \partial V$ at which the external source $S(\boldsymbol{r}, \boldsymbol{\Omega}) = 0$:

$$J^+ = \left(\frac{1}{4} + J_0\right)\left(\varphi_1 - \frac{2}{3}\varphi_2 + \frac{8}{15}\varphi_3 - \frac{16}{35}\varphi_4\right) - \left(\frac{0.5 + J_1}{3\mu_{a1}}\right)\boldsymbol{n} \cdot \nabla\varphi_1$$
$$+ \left(\frac{5}{16} + J_2\right)\left(\frac{1}{3}\varphi_2 - \frac{4}{15}\varphi_3 + \frac{8}{35}\varphi_4\right) - \left(\frac{J_3}{7\mu_{a3}}\right)\boldsymbol{n} \cdot \nabla\varphi_2 + \left(-\frac{3}{32} + J_4\right)\left(\frac{1}{5}\varphi_3 - \frac{6}{35}\varphi_4\right)$$
$$- \left(\frac{J_5}{11\mu_{a5}}\right)\boldsymbol{n} \cdot \nabla\varphi_3 + \left(\frac{13}{256} + J_6\right)\left(\frac{1}{7}\varphi_4\right) - \left(\frac{J_7}{15\mu_{a7}}\right)\boldsymbol{n} \cdot \nabla\varphi_4.$$

(32)

The SP_5 exiting partial current is obtained by setting $\phi_6 = 0$; the SP_3 exiting partial current is obtained by setting $\phi_6 = \phi_4 = 0$, and the SP_1 (diffusion) exiting partial current is obtained by setting $\phi_6 = \phi_4 = \phi_2 = 0$. Thus, the exiting partial current for the 3-D diffusion approximation is:

$$J^+(\boldsymbol{r}) = \left(\frac{1}{4} + J_0\right)\phi_0(\boldsymbol{r}) - \left(\frac{0.5 + J_1}{3\mu_{a1}(\boldsymbol{r})}\right)\boldsymbol{n} \cdot \nabla\phi_0(\boldsymbol{r}).$$

(33)

3.5. Solution methods

The SP_N equations for the composite moments φ_n are a system of coupled diffusion equations. These equations have a standard elliptic form, and many computationally efficient numerical solvers are available for solving them [40,41].

In our 2-D work, the diffusion equations are discretized using a standard finite-difference approach. The Legendre moments ϕ_n and the composite moments φ_n are defined on spatial grid points $\boldsymbol{r}_i = (x_i, y_i)$ of a 2-D Cartesian grid. The diffusion operators are approximated by *centered finite difference* approximations. This spatial discretization yields an algebraic system of coupled equations, which are solved by a *successive over-relaxation* (SOR) method. An over-relaxation parameter $\omega = 1$ yields the *Gauss–Seidel* method.

The ERT is an integro-differential equation with a five-dimensional phase space. All of the computational techniques available for solving this equation are expensive, demanding large amounts of computer memory and a long processing time. (This is the primary motivation for the work presented in this paper.) To obtain solutions of the ERT to which we can compare the SP_N solutions, we have adopted a straightforward approach: the spatial derivatives of the ERT are discretized by a first-order finite-difference scheme, termed the *step difference* (SD) method, or with a second-order finite-difference scheme, termed *diamond difference* (DD) scheme [42]; the angular variable $\boldsymbol{\Omega}$ and the integral term in Eq. (8) are discretized by discrete ordinates [15,43]. The resulting system of algebraic equations is iteratively solved by the Gauss–Seidel method with the source iteration (SI) technique. For more details we refer to [19].

The SP_N and diffusion equations are approximations to the equation of radiative transfer. Therefore, exact solutions derived from the SP_N and diffusion equations will exhibit inherent physical model errors σ_M when compared to exact solutions to the ERT. Besides the model errors σ_M, which depend on the particular type of

equation used for modeling the light propagation, we also have discretization errors, due to the use of a finite grid. (Moreover, exact solutions of the ERT are not available for complex tissue geometries and non-uniform distributions of optical properties, and our numerical estimates of the ERT solutions have their own discretization errors.) Consequently, a successful model error validation requires a sufficiently small discretization error. Therefore, we must (i) estimate the discretization error of our solution techniques for solving the ERT, and (ii) validate the physical model error of the SP_N and diffusion equations when compared to numerical solutions of the ERT. Numerical solutions of the ERT will subsequently be used as benchmark for validating the accuracy and computational performance of the SP_N method. We discuss the discretization errors σ_E in the next section, and the model errors σ_M later in Section 5.

4. Discretization error estimation of S_N method

The SP_N light propagation models used throughout our study are discretized using finite-difference methods, which approximate the spatial derivatives, e.g. the Laplacian and first-derivative operators, by finite difference approximations derived from truncated Taylor series expansions. The truncation of the Taylor series results in a truncation error. The application of a particular finite-difference approximations with different truncation error leads to numerical solutions with different accuracy. Furthermore, a convergence error is introduced due to the employment of iterative numerical solution techniques such as the Gauss–Seidel method and the source iteration method. Therefore, it is necessary to assess the numerical error of the S_N method before the validation of solutions of the SP_N and diffusion equations are carried out.

The most prevalent part of the numerical error when using finite difference methods is due to the Taylor series truncation of the finite-difference approximation [40,41]. The truncation error E is a function of the spatial step length Δx of adjacent grid points. The truncation error E_{SD} of the step difference approximation of the ERT is only first-order: $E_{SD} = O(\Delta x)$. Thus, the step difference (SD) method generally requires very fine Cartesian grids for yielding solutions with sufficient accuracy. On the other hand, the diamond difference (DD) method has a second-order truncation error: $E_{DD} = O(\Delta x^2)$. This enables us to use coarser grids for yielding a similar numerical accuracy. However, a downside of the DD method is that it can produce unphysical oscillating solutions [42,44]. The truncation error of the centered finite-difference approximation of the SP_N and diffusion equations is also $O(\Delta x^2)$. Therefore, in principle, we can use similar Cartesian grids for solving the diffusion, SP_N, and diamond-differenced radiative transfer equations.

To validate our 2-D code, we ran it in 1-D mode and compared the solutions to those of a different independently-validated 1-D benchmark code with a S_{32} quadrature set and DD scheme. Our S_N code employed either the SD or DD scheme in conjunction with a S_{16} quadrature set. We define the numerical error σ_E as the average deviation of our S_N solutions ϕ from the 1-D S_{32} solution $\tilde{\phi}$ at all I grid points along the 1-D Cartesian grid:

$$\sigma_E = \sqrt{\frac{1}{I} \sum_{i}^{I} \left(\frac{\phi_i - \tilde{\phi}_i}{\tilde{\phi}_i}\right)^2} \times 100\%. \tag{34}$$

The quantities ϕ_i and $\tilde{\phi}_i$ constitute the fluence of the solution under consideration at a grid point i.

The numerical error σ_E of our S_N solutions with respect to the 1-D benchmark solutions substantially increased when the absorption coefficient μ_a and optical thickness were increased. We found that the SD scheme requires a spatial grid size $\Delta x < 0.02$ mfp for highly absorbing domains to obtain numerical errors less than 2% (see Table 1). These results encouraged us to use our S_N code and SD scheme – with very fine spatial grids – for benchmark calculations to validate the SP_N methods.

5. Methods

We performed numerical experiments to evaluate the computational performance and numerical accuracy of the SP_N methods. We demonstrate their suitable application as a light propagation model for biological tissue by choosing appropriate numerical tissue models. In particular, we considered optical parameters at visible and near-infrared wavelengths, covering a wide range of absorption coefficients. We also studied the

Table 1
Numerical error σ_E of fluence ϕ obtained from our S_N methods with (i) step-differencing (SD) scheme and (ii) diamond-differencing (DD) scheme as a function of the spatial separation Δx of adjacent grid points

Δx (cm)	mfp (cm)	tmfp (cm)	Optical thickness (mfp)	μ_s (cm^{-1})	g (n.u.)	μ_a (cm^{-1})	σ_E (SD) (%)	σ_E (DD) (%)
0.001389	0.0999	0.0999	10.01	10	0	0.01	0.18	0.33
0.001389	0.0909	0.0909	11	10	0	1	2.14	0.52
0.001389	0.0399	0.1996	25.01	25	0.8	0.01	0.69	0.75
0.002778	0.0999	0.0999	20.02	10	0	0.01	0.36	0.36
0.002778	0.0909	0.0909	22	10	0	1	8.53	0.88
0.002778	0.0399	0.1996	50.02	25	0.8	0.01	0.55	0.53
0.008334	0.0999	0.0999	20.02	10	0	0.01	0.92	0.97
0.008334	0.0909	0.0909	22	10	0	1	27.11	2.36
0.008334	0.0399	0.1996	50.02	25	0.8	0.01	0.69	0.86

The 1-D medium had different optical parameters and optical thickness. The benchmark method is an independently-validated 1-D S_N code with S_{32} quadrature set and DD scheme.

impact of small tissue geometries on the accuracy of the SP_N solutions. The numerical solutions of the SP_N methods were compared to solutions of the diffusion equation and to solutions of our validated S_N code with the SD scheme. The S_N solutions serve as a benchmark throughout our numerical study. Our numerical studies for validating the SP_N solutions are similar to studies of neutronic scattering problems that have been performed in nuclear engineering [22,23,25,27].

We used two different physical models, with sizes of 1 cm × 1 cm and 2 cm × 2 cm, mimicking the scattering and absorption physics of an 2-D transverse tissue slice of a small animal with typical optical parameters at visible and near-infrared wavelengths. A single isotropic light source with spatial size of 0.2 cm was symmetrically placed at the left hand side of the medium boundary ($x = 0$ cm). The small model with a cross-sectional area of only 1 cm² enabled us to study the impact of small tissue geometries on the accuracy of the SP_N solutions. Here, we presumed that boundary effects would dominate the light propagation, resulting in different solutions for the SP_N and diffusion equations. This case study is relevant in tomographic imaging of small tissue geometries, e.g. the brain in rats [45,46]. The second model has a four-times larger spatial cross-sectional area of 4 cm². Boundary effects here should be minimal, due to the increased tissue-volume to tissue-boundary ratio. This model is primarily used for studying the impact of large absorption coefficients, which is relevant in optical molecular imaging of fluorescent and bioluminescent probes emitting light at visible wavelengths [11,12].

In both models, the target medium is homogeneous. We conducted different numerical experiments while varying the scattering coefficients from 10 to 50 cm⁻¹, the absorption coefficient from 0.01 to 2 cm⁻¹, and the anisotropy factor from 0 to 0.8. In this way, we were able to study the impact of large tissue absorption and anisotropic scattering on the accuracy of the SP_N solutions. We expected a good match between all solutions (diffusion, SP_N, S_N) in optically thick media with a diffusive regime where $\mu'_s \gg \mu_a$ holds. But, we anticipated larger deviations between the diffusion and S_N solutions in media with large absorption coefficients and in optically thin media near the boundary. All numerical experiments were carried out for either non-reentry ($n_m = 1$) or partially-reflective ($n_m = 1.37$) boundary conditions (see Fig. 1).

The SP_N and the diffusion equations were solved on Cartesian grids with spatial grid point separation of 0.008333 cm for both models. Therefore, a 121 × 121 grid, as shown in Fig. 2a, modeled the 1 cm × 1 cm medium, and a 241 × 241 grid modeled the 2 cm × 2 cm medium. The Cartesian grids of the S_N simulations had a smaller cell size of only 0.001389 cm between adjacent grid points in order to alleviate the impact of the numerical error σ_E originating from the SD scheme (see Table 1). Hence, we needed to employ Cartesian grids with 721 × 721 and 1441 × 1441 grid points, as shown in Fig. 2b. Only for low-absorbing media could we also use a larger grid point separation of 0.002778 cm and the 721 × 721 grid.

For processing time evaluations, the S_N equations were also solved by using the DD scheme. Therefore, the S_N method with DD scheme could be employed on coarser Cartesian grids with same size as used for solving the diffusion and SP_N equations. However, the DD scheme does not always produce physically meaningful solutions [15,42,43], and only SD solutions were available for cases with large absorption coefficients.

The solutions of the diffusion and SPN equations on the 121 × 121 grids were compared to solutions of the ERT obtained with an S_{16} method (288 discrete ordinates) on the 721 × 721 grid. The solutions of the diffusion

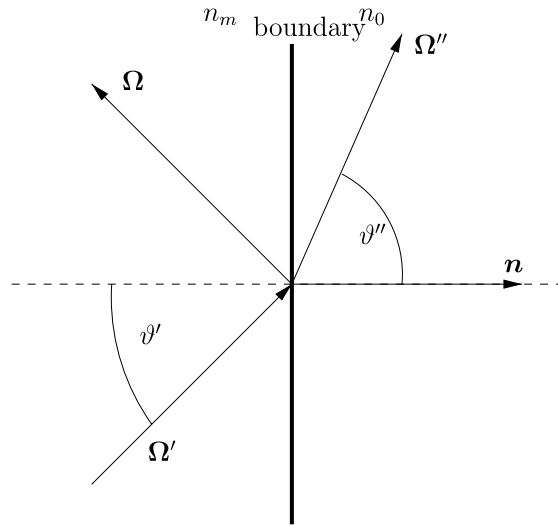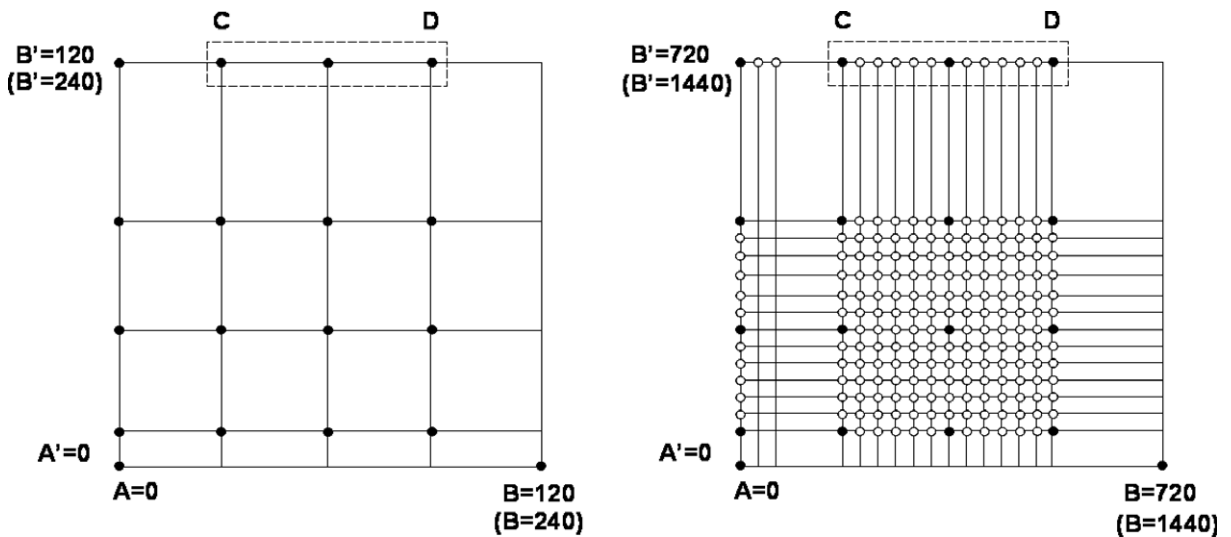Fig. 1. Light leaving the medium (refractive index n_m) along the outward direction $\mathbf{\Omega}'$ is reflected back into the medium along $\mathbf{\Omega}$ and refracted along $\mathbf{\Omega}''$ into the outside medium (refractive index n_0).

(a) Coarse grid with either 121×121 or 241×241 grid points.

(b) Fine grid with either 721×721 or 1441×1441 grid points.

Fig. 2. Cartesian grids with different amount of grid points. The coarse grids (a) are used for solving the SP_N and diffusion equations, whereas the fine grids (b) are used for solving the S_N equations with the SD scheme.

and SP_N calculations on the 241×241 grids were compared to solutions of the ERT obtained with an S_6 method (48 discrete ordinates) on a 1441×1441 grid. We could only use an S_6 approximation for the 1441×1441 grid, due to the limited computational capabilities of our 32-bit processor. (This can manage an address space of four GBytes, but our S_{16} method on a 1441×1441 grid requires more than nine GBytes storage.) Therefore, we were not able to model anisotropically scattering media on fine spatial grids.

Moreover, we were not able to model partially-reflective boundary conditions when using the 1441×1441 grid with the S_6 quadrature set. The reflectivity $R(\vartheta')$ (Eq. (5)) is a strongly varying function for $n_m > 1$ and $\vartheta' < \vartheta_c$. Hence, the discretization of R requires a sufficiently large number of discrete ordinates. We found that an S_6 quadrature set is not sufficient to obtain accurate numerical results for partial reflection.

Fig. 2 shows both fine and coarse Cartesian grids. The medium boundary is, for example, along the line between the points (A, B) and (A', B'). The line (A', B') depicts the x-axis and line (A, B) depicts the y-axis. Boundary grid points, such as grid points A, C, etc., are exactly located at the physical medium boundary. We obtain the fine grid by placing additional grid points (white circles in Fig. 2b) in between grid points of the coarse grid (black circles in Fig. 2a). Consequently, the spatial separation between adjacent grid points of the fine grid is only one sixth the spatial separation of the coarse grid. The source is extended along the line between the points (C, D) at the medium boundary. We allocated 25 grid points as source points in the coarse grid, and 145 grid points as source points in the fine grid. The dashed rectangle in both figures encloses all source points.

5.1. Model error of fluence and partial current

The SP_N and diffusion solutions are compared to our S_N benchmark solutions in order to quantify the physical model error σ_M of each individual method. The S_N method employed the SD scheme and 288 discrete ordinates (S_{16}). The fluence ϕ was calculated at all interior grid points, whereas the partial current J^+ was only calculated at boundary grid points. The model error of the fluence σ_{Mi}^ϕ inside the medium is taken at an interior grid point i along the x-axis, starting from the source location towards the opposite medium boundary. It is calculated by taking the relative difference at a mutual grid point i of the fluence ϕ_i of the SP_N or diffusion method with respect to the fluence $\tilde{\phi}_i$ of the S_N method:

$$\sigma_{Mi}^\phi = \frac{\phi_i - \tilde{\phi}_i}{\tilde{\phi}_i} \times 100\%. \tag{35}$$

The model error $\sigma_{Mi}^{J^+}$ of the partial current J^+ is taken at each mutual boundary grid point i along the y-axis on the side opposite to the source. We did not include boundary points in the proximity of medium corners, because we presume larger model errors of the benchmark method.

$$\sigma_{Mi}^{J^+} = \frac{J_i^+ - \tilde{J}_i^+}{\tilde{J}_i^+} \times 100\%. \tag{36}$$

The model errors $\sigma_{Mi}^{J^+, \phi}$ at each individual grid point is shown in Figs. 3–18 for the fluence ϕ and the partial current J^+. The total model errors $\sigma_M^{J^+, \phi}$ of the partial current and fluence at I mutual interior grid points and I_B mutual boundary grid points on the opposite side to the source location are defined as
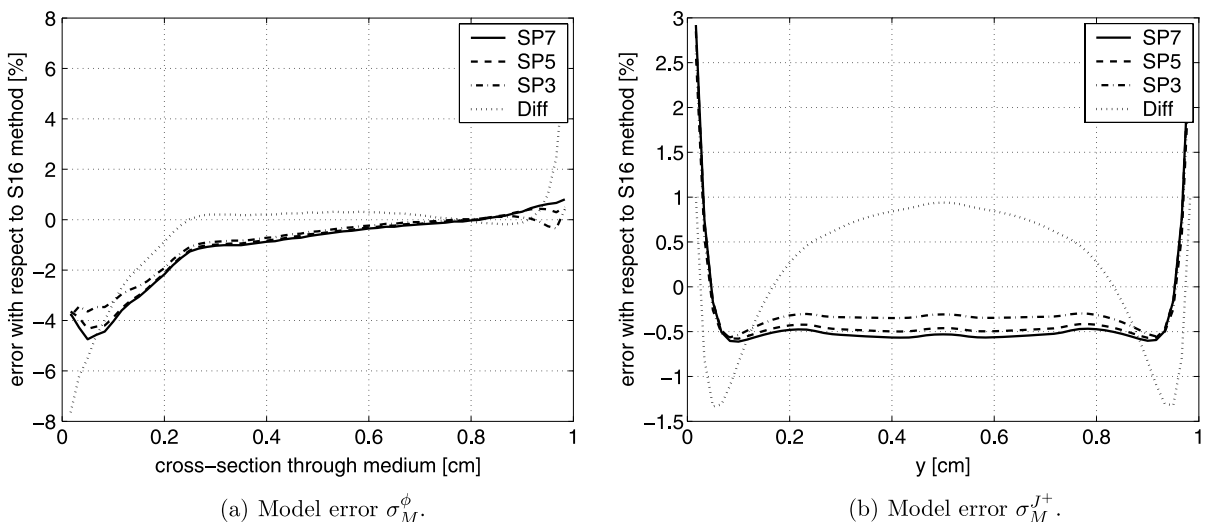

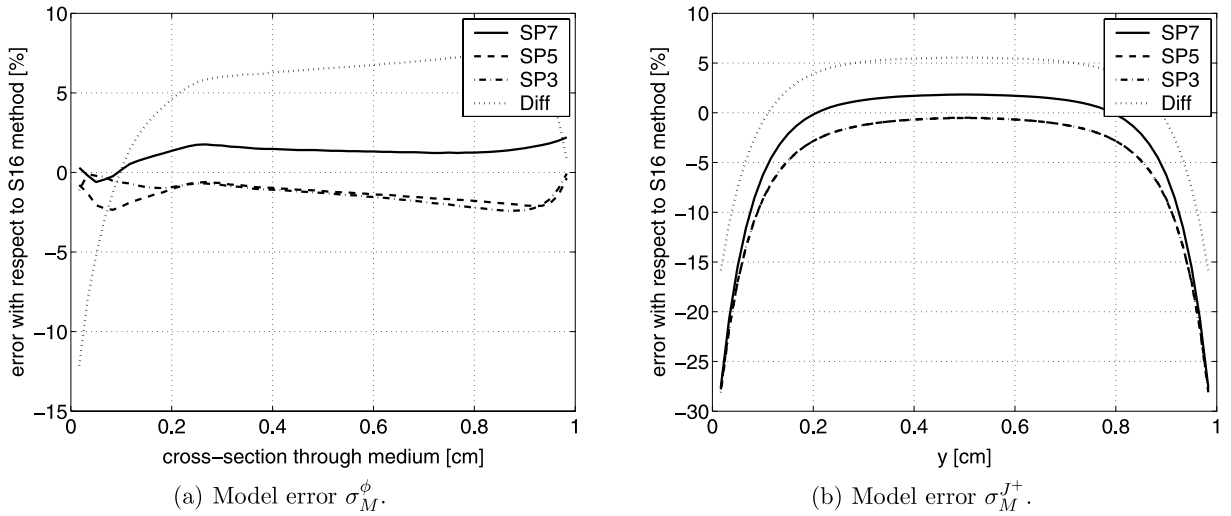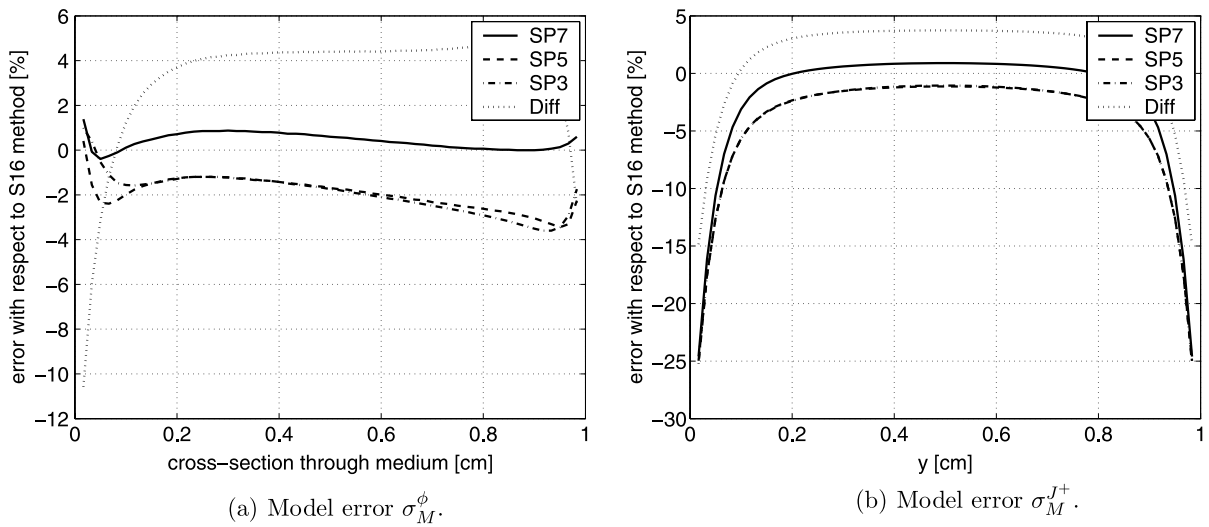(a) Model error σ_M^ϕ.　　　　　　(b) Model error $\sigma_M^{J^+}$.

Fig. 3. Case 1: Model errors of (a) fluence ϕ along x-axis through medium center ($y = 0.5$ cm) and of (b) partial current J^+ along y-axis at medium boundary opposite to source ($x = 1$ cm). Optical properties: $\mu_s = 10$ cm^{-1}, $\mu_a = 0.01$ cm^{-1}, $g = 0$, $n_m = 1$.

(a) Model error σ_M^ϕ.   (b) Model error $\sigma_M^{J^+}$.

Fig. 4. Case 2: Model errors of (a) fluence ϕ along x-axis through medium center ($y = 0.5$ cm) and of (b) partial current J^+ along y-axis at medium boundary opposite to source ($x = 1$ cm). Optical properties: $\mu_s = 10$ cm^{-1}, $\mu_a = 0.01$ cm^{-1}, $g = 0$, $n_m = 1.37$.

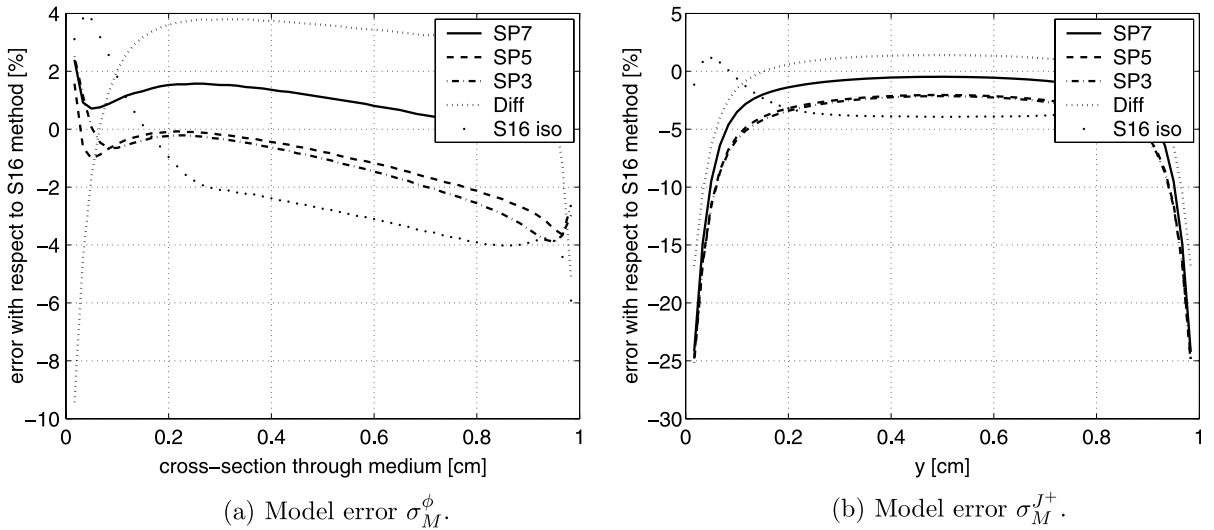(a) Model error σ_M^ϕ.   (b) Model error $\sigma_M^{J^+}$.

Fig. 5. Case 3: Model errors of (a) fluence ϕ along x-axis through medium center ($y = 0.5$ cm) and of (b) partial current J^+ along y-axis at medium boundary opposite to source ($x = 1$ cm). Optical properties: $\mu_s = 20$ cm^{-1}, $\mu_a = 0.01$ cm^{-1}, $g = 0.5$, $n_m = 1.37$.

$$\sigma_M^{J^+} = \sqrt{\frac{1}{I_B} \sum_i^{I_B} \left(\frac{J_i^+ - \widetilde{J}_i^+}{\widetilde{J}_i^+} \right)^2} \times 100\%, \tag{37}$$

$$\sigma_M^\phi = \sqrt{\frac{1}{I} \sum_i^{I} \left(\frac{\phi_i - \tilde{\phi}_i}{\tilde{\phi}_i} \right)^2} \times 100\%. \tag{38}$$

We show the total model error σ_M^ϕ and $\sigma_M^{J^+}$ of the fluence and partial current in Tables 2, 3, 5, and 6.

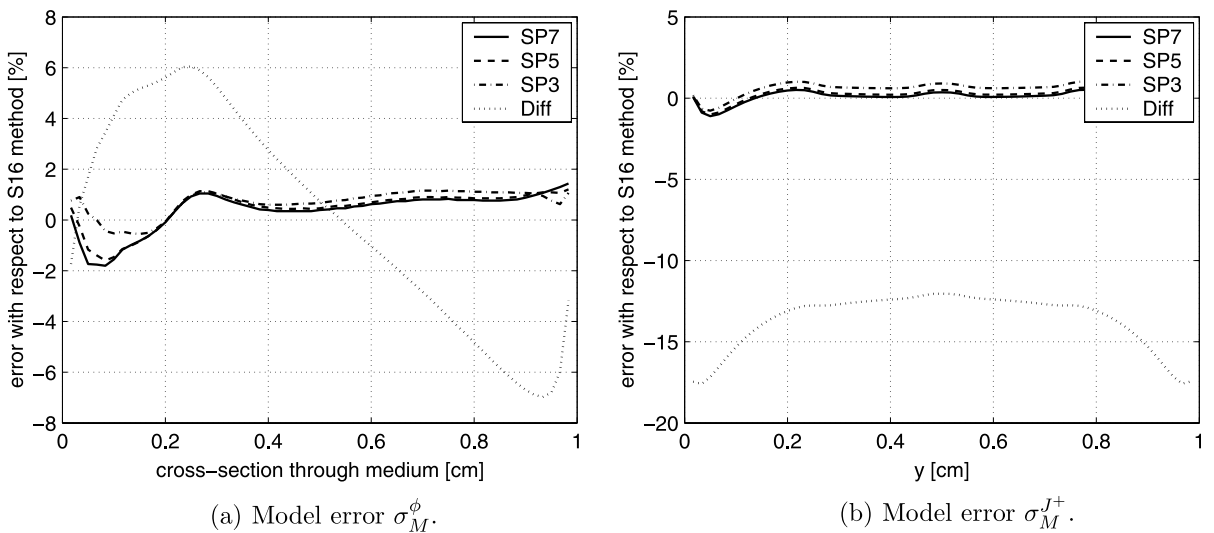(a) Model error σ_M^ϕ. (b) Model error $\sigma_M^{J^+}$.

Fig. 6. Case 4: Model errors of (a) fluence ϕ along x-axis through medium center ($y = 0.5$ cm) and of (b) partial current J^+ along y-axis at medium boundary opposite to source ($x = 1$ cm). Optical properties: $\mu_s = 50$ cm^{-1}, $\mu_a = 0.01$ cm^{-1}, $g = 0.8$, $n_m = 1.37$. `S16 iso` represents the solution of the isotropically-scattering ERT (Eq. (39)).

(a) Model error σ_M^ϕ. (b) Model error $\sigma_M^{J^+}$.

Fig. 7. Case 5: Model errors of (a) fluence ϕ along x-axis through medium center ($y = 0.5$ cm) and of (b) partial current J^+ along y-axis at medium boundary opposite to source ($x = 1$ cm). Optical properties: $\mu_s = 10$ cm^{-1}, $\mu_a = 1$ cm^{-1}, $g = 0$, $n_m = 1$.

5.2. Processing time

Another performance measure besides the model error σ_M is the relative processing time T for achieving the numerical solutions. The iterative solvers for the diffusion, SP_N, and S_N equations used a stop criterion $\frac{\phi^{l+1} - \phi^l}{\phi^l} < 10^{-6}$ of the fluence ϕ at consecutive iteration steps l and $l + 1$. The number of iteration steps after the calculation has been completed, i.e. satisfying the stopping criterion, determined the total processing time. We decided to compare the processing time of solving the SP_N and S_N equations to the time needed for completing the diffusion calculation. The diffusion model is the most widely used light propagation model in tissue optics and, hence, it is reasonable to use it as a benchmark for processing time. We compared the relative
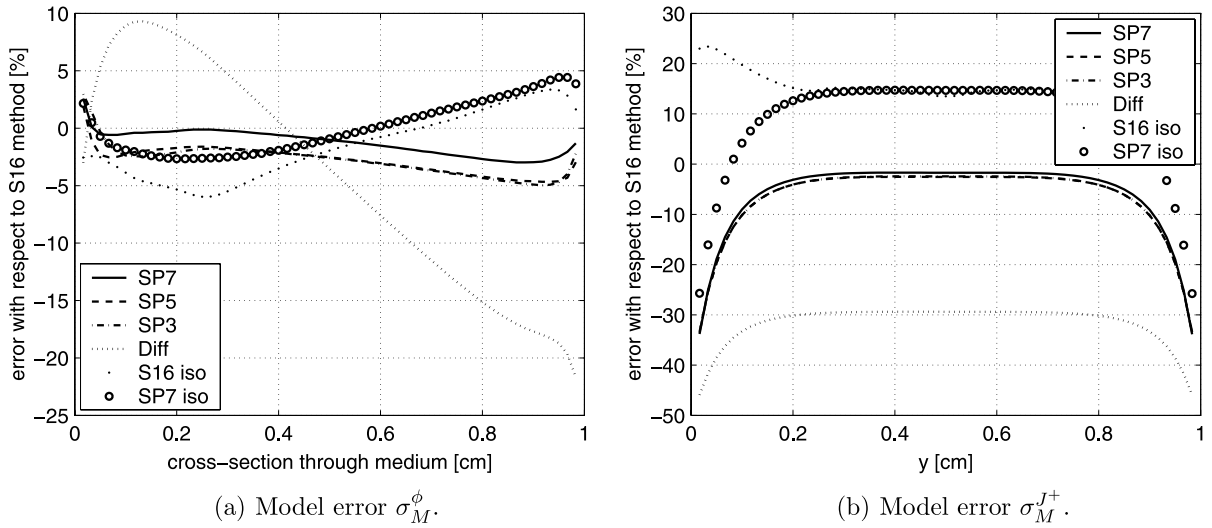
Fig. 8. Case 6: Model errors of (a) fluence ϕ along x-axis through medium center ($y = 0.5$ cm) and of (b) partial current J^+ along y-axis at medium boundary opposite to source ($x = 1$ cm). Optical properties: $\mu_s = 20$ cm^{-1}, $\mu_a = 2$ cm^{-1}, $g = 0.5$, $n_m = 1.37$. S16 iso and SP7 iso represent the solutions of the isotropically-scattering ERT (Eq. (39)) and the SP_7 equation for $g = 0$.
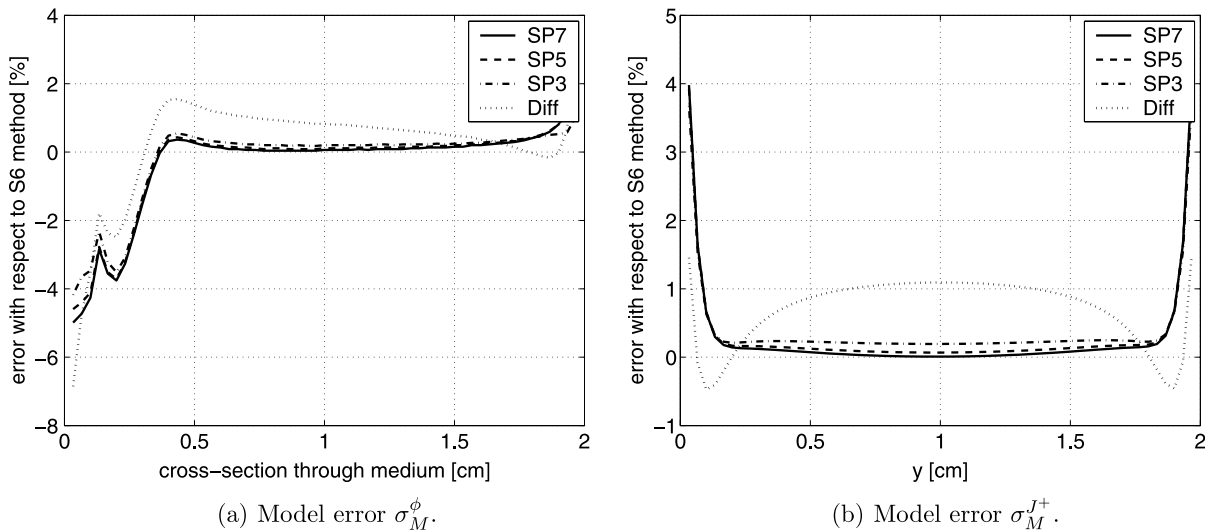

Fig. 9. Case 7: Model errors of (a) fluence ϕ along x-axis through medium center ($y = 1$ cm) and of (b) partial current J^+ along y-axis at medium boundary opposite to source ($x = 2$ cm). Optical properties: $\mu_s = 10$ cm^{-1}, $\mu_a = 0.01$ cm^{-1}, $g = 0$, $n_m = 1$.

speed of all methods for each numerical example by assigning the same unit time to each diffusion calculation. By doing so, the measure of performance, the relative processing time T, is independent of the used processor type. The relative processing time T of all numerical examples is given in Tables 4 and 7, with $T(P_1) = 1$ being the processing time of the diffusion method.

Our S_N code for tissue optics is not optimized for time performance, so the given timing comparison of our SP_N methods to the S_N method is not likely to be an objective measure of time performance for optimized codes. Therefore, we further estimate in Section 7, as an additional performance measure, the relative processing time of our SP_N methods to processing times of optimized diffusion and S_N codes as they are employed in nuclear engineering codes.
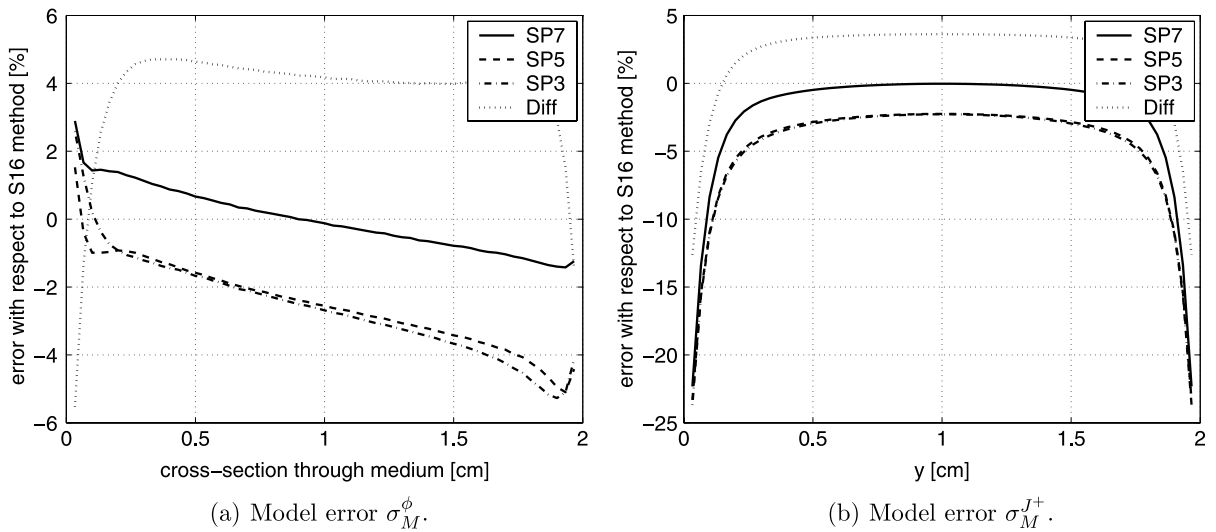
(a) Model error σ_M^ϕ.

(b) Model error $\sigma_M^{J^+}$.

Fig. 10. Case 8: Model errors of (a) fluence ϕ along x-axis through medium center ($y = 1$ cm) and of (b) partial current J^+ along y-axis at medium boundary opposite to source ($x = 2$ cm). Optical properties: $\mu_s = 10$ cm^{-1}, $\mu_a = 0.01$ cm^{-1}, $g = 0$, $n_m = 1.37$.

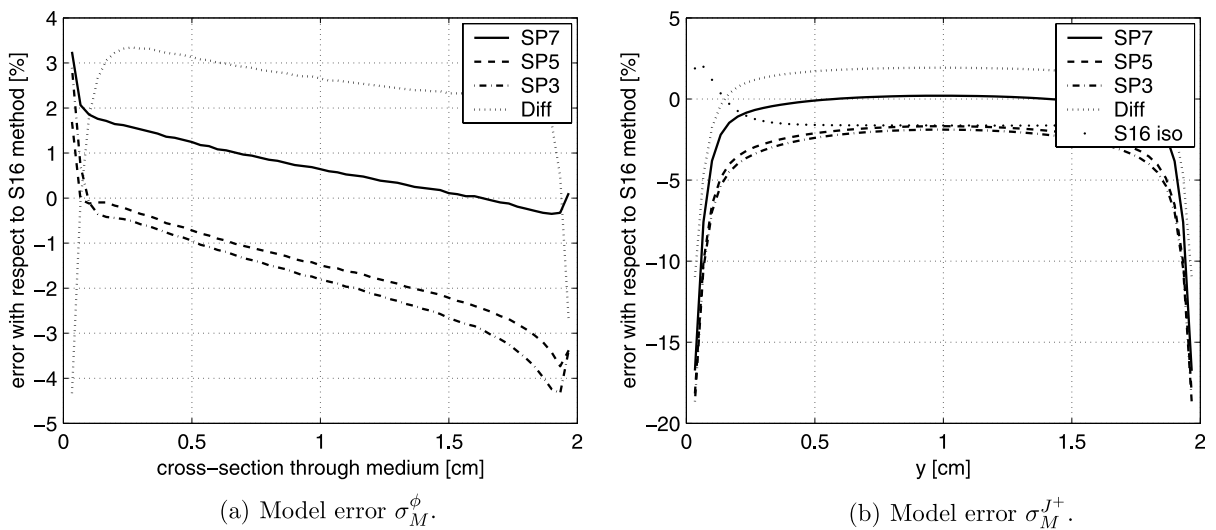(a) Model error σ_M^ϕ.

(b) Model error $\sigma_M^{J^+}$.

Fig. 11. Case 9: Model errors of (a) fluence ϕ along x-axis through medium center ($y = 1$ cm) and of (b) partial current J^+ along y-axis at medium boundary opposite to source ($x = 2$ cm). Optical properties: $\mu_s = 20$ cm^{-1}, $\mu_a = 0.01$ cm^{-1}, $g = 0.5$, $n_m = 1.37$.

6. Results

6.1. Size: 1 cm × 1 cm

We defined six tissue-like media (cases 1–6) with different levels of absorption, ranging from 0.01 to 2 cm^{-1}. Also, we kept the reduced scattering coefficient $\mu_s' = (1 - g)\mu_s = 10$ cm^{-1} constant, but varied the scattering coefficient μ_s from 10 to 50 cm^{-1} and the anisotropy factor g from 0 to 0.8. The calculations of the SP_N and diffusion methods were performed on the 121×121 grid, whereas the S_{16} benchmark method run on the 721×721 grid. We display in Figs. 3–8 the model errors σ_M of the fluence ϕ inside the medium along the x-axis, and of the partial current J^+ at the medium boundary along the y-axis opposite to the source. The total model error and processing time of all methods are given in Tables 2–4.
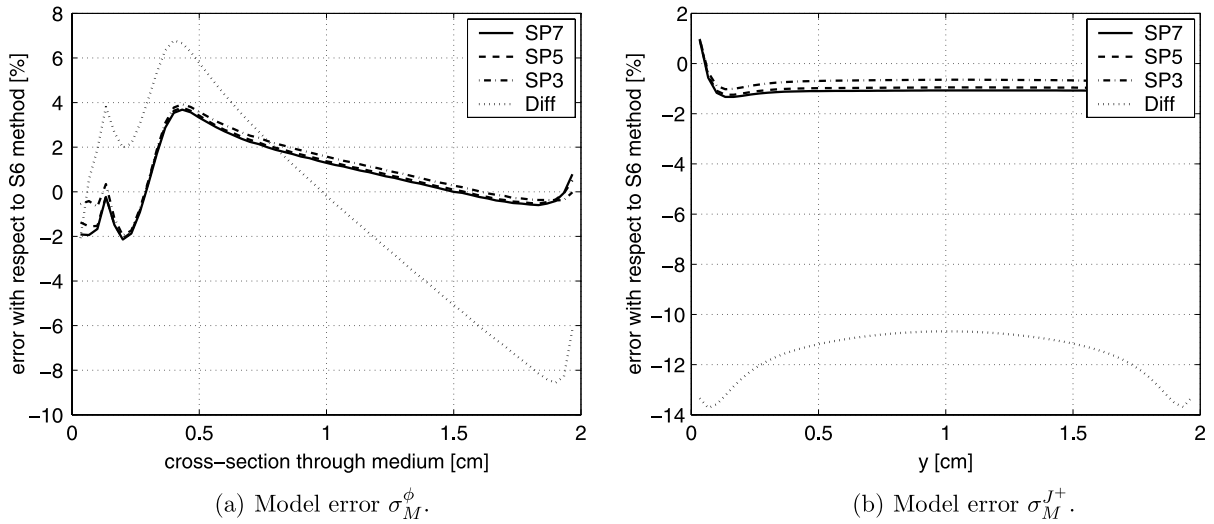
(a) Model error σ_M^ϕ.   (b) Model error $\sigma_M^{J^+}$.

Fig. 12. Case 10: Model errors of (a) fluence ϕ along x-axis through medium center ($y = 1$ cm) and of (b) partial current J^+ along y-axis at medium boundary opposite to source ($x = 2$ cm). Optical properties: $\mu_s = 10$ cm^{-1}, $\mu_a = 0.5$ cm^{-1}, $g = 0$, $n_m = 1$.

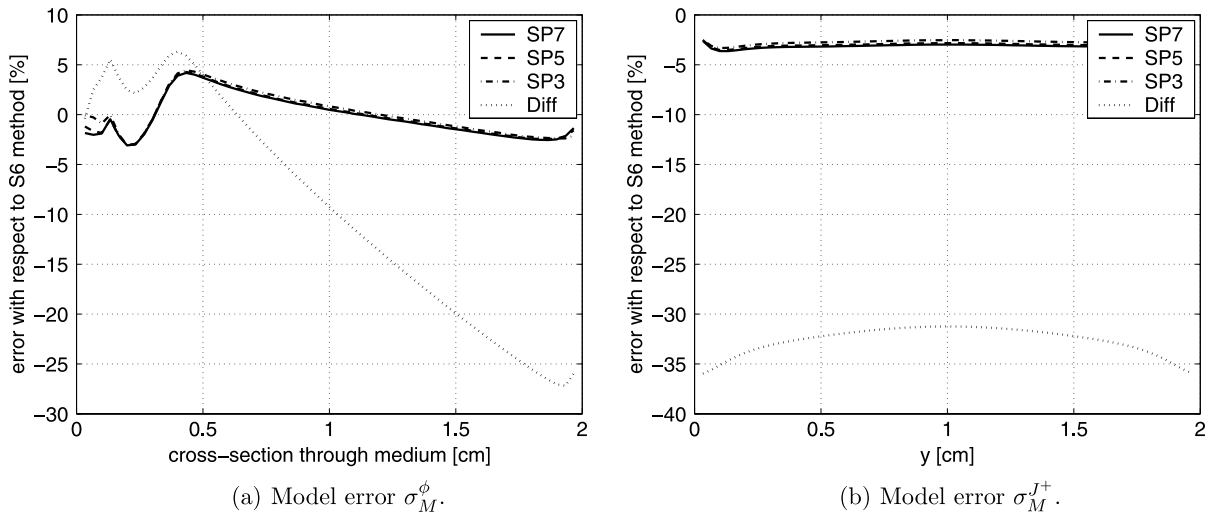(a) Model error σ_M^ϕ.   (b) Model error $\sigma_M^{J^+}$.

Fig. 13. Case 11: Model errors of (a) fluence ϕ along x-axis through medium center ($y = 1$ cm) and of (b) partial current J^+ along y-axis at medium boundary opposite to source ($x = 2$ cm). Optical properties: $\mu_s = 10$ cm^{-1}, $\mu_a = 1$ cm^{-1}, $g = 0$, $n_m = 1$.

Case 1 is an isotropically scattering medium with $\mu_s = 10$ cm^{-1}, $\mu_a = 0.01$ cm^{-1}, $g = 0$, and non-reentry boundary conditions ($n_m = 1$). We see a relatively good agreement between all solutions. The model error σ_M of all methods is in the range of the numerical error σ_E of our S_{16} benchmark solution with respect to the 1-D S_{32} solution (see Table 1). But, the model error σ_M slightly increases for partially reflective boundary conditions ($n_m = 1.37$) as considered in case 2. In case 3 we defined an anisotropically scattering medium with $g = 0.5$ and $\mu_s = 20$ cm^{-1} with partially reflective boundary conditions ($n_m = 1.37$), but keeping $\mu_s' = 10$ cm^{-1} constant. The model error only slightly changes for all SP_N methods, indicating a minor impact of anisotropic scattering in diffusive regimes with $\mu_s' \gg \mu_a$. The largest change in the model error for small absorption coefficients could only be seen when introducing partially reflective boundary conditions.

In cases 5 and 6 we increased the absorption coefficient to $\mu_a = 1$ cm^{-1} and $\mu_a = 2$ cm^{-1}, i.e. shifting towards visible wavelengths. We see a significant increase in the model error σ_M for the diffusion solution. However, the model error of the SP_N solutions remains relatively small, with $\sigma_M = 2$–4%.

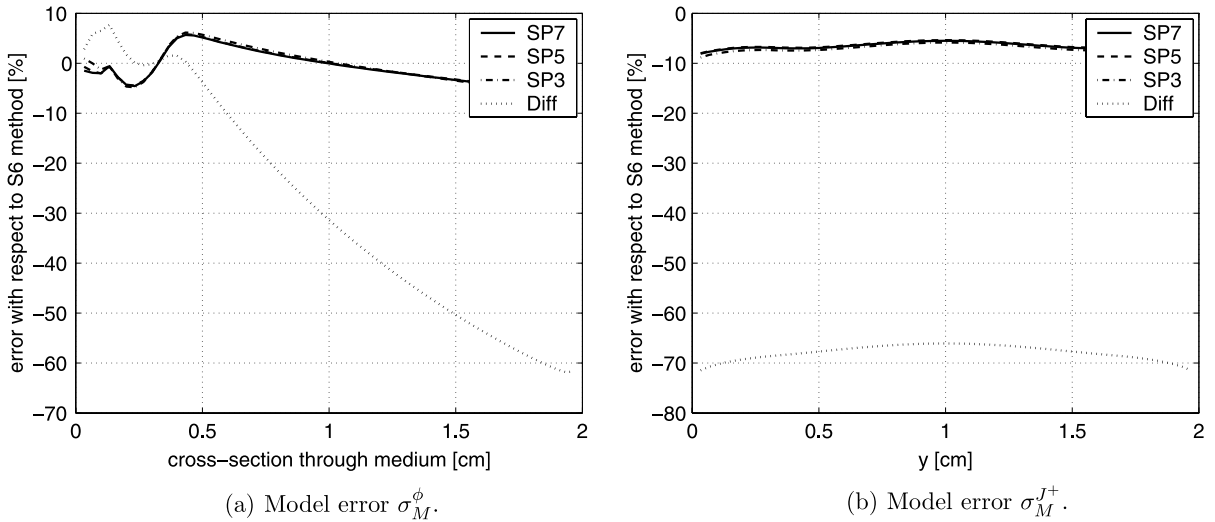(a) Model error σ_M^{ϕ}.

(b) Model error $\sigma_M^{J^+}$.

Fig. 14. Case 12: Model errors of (a) fluence ϕ along x-axis through medium center ($y = 1$ cm) and of (b) partial current J^+ along y-axis at medium boundary opposite to source ($x = 2$ cm). Optical properties: $\mu_s = 10 \text{ cm}^{-1}$, $\mu_a = 2 \text{ cm}^{-1}$, $g = 0$, $n_m = 1$.

In Fig. 6 we also compare the S_{16} solution of the ERT with anisotropic scattering (Eq. (1)) to the S_{16} solution of the isotropically-scattering ERT as given by:

$$\mathbf{\Omega} \cdot \nabla \psi(\mathbf{r}, \mathbf{\Omega}) + [\mu_a(\mathbf{r}) + (1 - g)\mu_s(\mathbf{r})]\psi(\mathbf{r}, \mathbf{\Omega}) = \left[\frac{(1 - g)\mu_s(\mathbf{r})}{4\pi}\right] \int_{4\pi} \psi(\mathbf{r}, \mathbf{\Omega}') \, d\Omega' + \frac{Q(\mathbf{r})}{4\pi}. \tag{39}$$

Both ERTs have the same diffusion approximation, but have different SP_N and S_N solutions. In our numerical study, we found that the S_{16} solution of the isotropically-scattering equation (39) closely approximates the S_{16} solution of the anisotropically-scattering equation (1). The model error σ_M of the isotropically-scattering ERT is less than 4%.

However, as the problem becomes less diffusive, the solutions of the two ERTs begin to differ. In Fig. 8 we included solutions of the isotropically-scattering ERT and of the SP_7 equations for an isotropically scattering medium with $g = 0$ and $\mu_s' = 10 \text{ cm}^{-1}$. Both solutions are similar but show relatively large models errors, e.g. $\sigma_M^{J^+} = 15\%$, when compared to the S_N and SP_7 solutions of the anisotropically scattering medium with $g = 0.5$. Thus, the accurate modeling of anisotropic scattering gains importance in highly absorbing media.

6.2. Size: 2 cm × 2 cm

We also studied the physical model error σ_M of the SP_N and diffusion methods for the optically thick medium with size of 2 cm × 2 cm. The optical parameters, μ_s, g, and μ_a, were varied for six different media while keeping $\mu_s' = 10 \text{ cm}^{-1}$ constant (cases 7–12). As before, we calculated the fluence ϕ inside the medium along the x-axis, and the partial current J^+ at the medium boundary along the y-axis opposite the source location.

The calculations for cases 7–9 were performed on a 121×121 grid for the SP_N and diffusion methods, whereas the S_{16} method employed the 721×721 grid. Cases 10–12 deal with highly absorbing media, requiring finer Cartesian grids due to the increased numerical error σ_E of our S_N benchmark approach (see Table 1). Therefore, the S_6 transport method ran on a 1441×1441 grid, whereas the diffusion and SP_N equations were solved on a 241×241 grid. Cases 10–12 did not model anisotropically scattering media with partially reflective boundary conditions, due to the small S_6 quadrature set.

Case 7 is an isotropically scattering medium with $\mu_s = 10 \text{ cm}^{-1}$, $g = 0$, $\mu_a = 0.01 \text{ cm}^{-1}$, and non-reentry boundary conditions ($n_m = 1$). We anticipated a good match of all SP_N and diffusion solutions and a relatively small model error due to the diffusive regime holding $\mu_s' \gg \mu_a$. The actual model error σ_M of all methods is less than 1%, being in the range of the numerical error σ_E of the S_{16} transport solution with respect to the 1-D S_{32} benchmark solution (see Table 1). Case 8 is similar to case 7, except that partially reflective boundary condi-
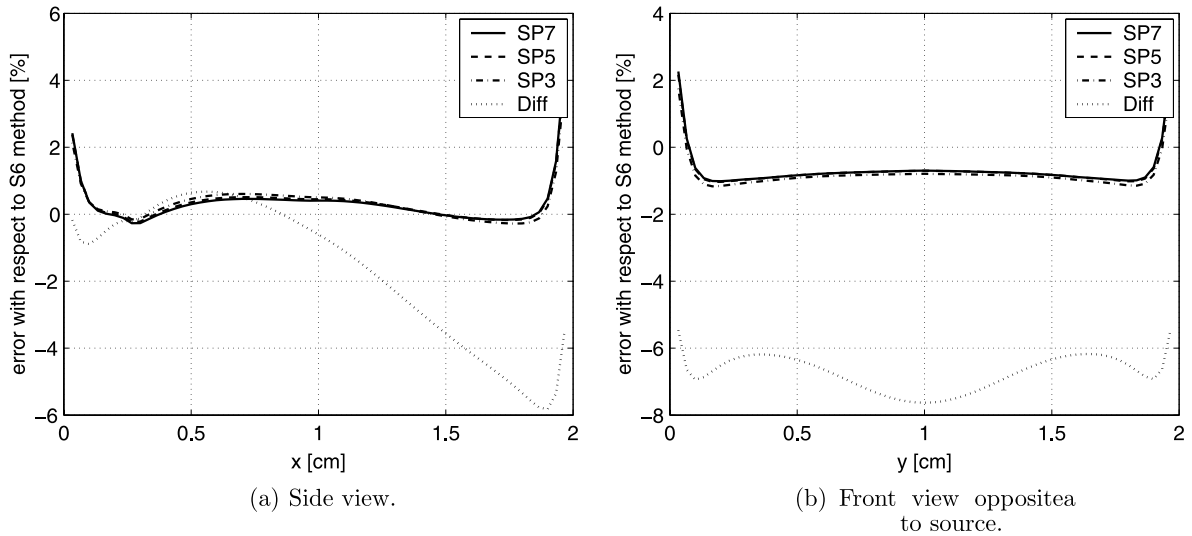
(a) Side view.   (b) Front view oppositea
                                                  to source.

Fig. 15. Case 13: Model error $\sigma_M^{J^+}$ of partial current J^+ at medium boundaries (a) along x-axis at $y = 0$ cm (side view) and (b) along y-axis at $x = 2$ cm (front view opposite to source). Optical properties: $\mu_s = 10$ cm^{-1}, $\mu_a = 0.01$ cm^{-1}, $g = 0$, $n_m = 1$. A single absorber ($\mu_a = 2$ cm^{-1}) with diameter 0.6 cm was placed at center $(x,y) = (1,1)$.

(a) σ_M^ϕ of diffusion solution.   (b) σ_M^ϕ of SP_3 solution.
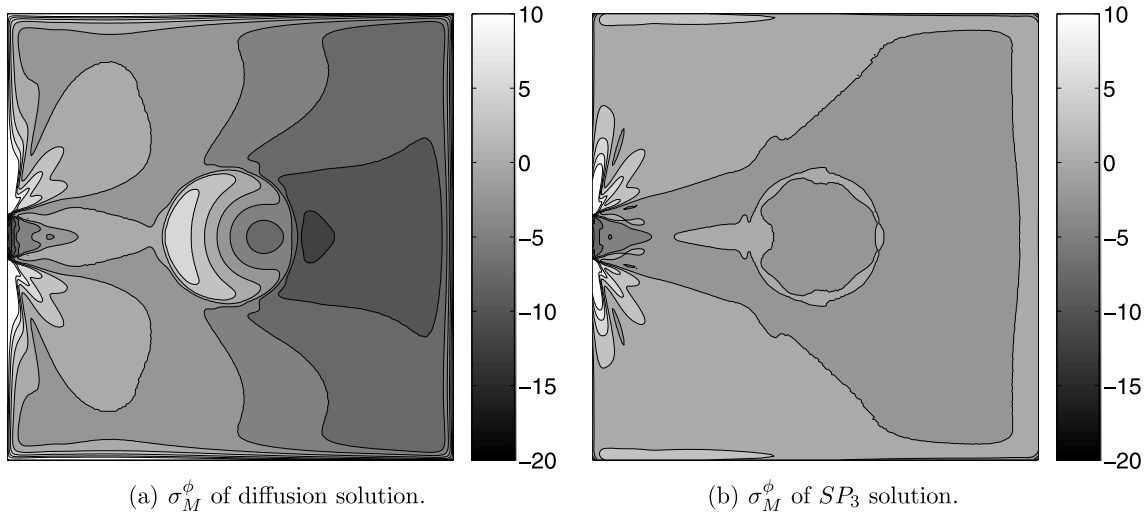
Fig. 16. Case 13: 2-D spatial distribution of model error σ_M^ϕ in (%) of fluence derived from (a) diffusion solution and (b) SP_3 solution with respect to fluence of S_6 solution. Source position is at the center on the left-hand side. Optical properties: $\mu_s = 10$ cm^{-1}, $\mu_a = 0.01$ cm^{-1}, $g = 0$, $n_m = 1$. A single absorber ($\mu_a = 2$ cm^{-1}) with diameter 0.6 cm was placed at center $(x,y) = (1,1)$.

tions ($n_m = 1.37$) were used. This example allows us to study the impact of boundary conditions with refractive index mismatch as found at tissue–air interfaces. We found the largest model error $\sigma_M^{J^+}$ of 3.45% for the diffusion solution, but the smallest error was at 0.44% for the SP_7 solution. Case 9 studies the impact of anisotropic scattering on the model error. The scattering coefficient was $\mu_s = 20$ cm^{-1}, whereas the anisotropy factor was set to $g = 0.5$, while keeping μ_s' constant. We anticipated that case 9 would give similar results as case 8, due to the diffusive regime.

Cases 10–12 consider isotropically scattering media with non-reentry boundary conditions ($n_m = 1$). We varied the absorption coefficient, 0.5, 1, and 2 cm^{-1}, shifting towards wavelengths of visible light. All three cases show a gradually increased model error for the diffusion solution, the largest being at $\sigma_M^{J^+} = 68\%$. The largest model error $\sigma_M^{J^+}$ of all SP_N solutions was less than 6%. The model error of the partial current was twice the error of the fluence inside the medium.
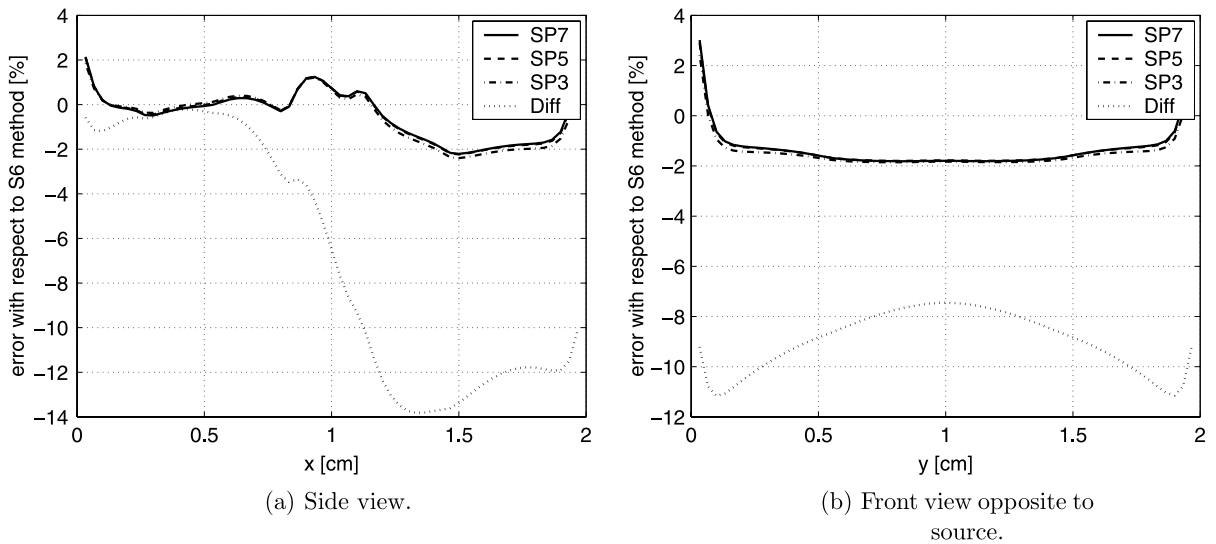
(a) Side view.

(b) Front view opposite to
source.

Fig. 17. Case 14: Model error $\sigma_M^{J^+}$ of partial current J^+ at medium boundaries (a) along x-axis at $y = 0$ cm (side view) and (b) along y-axis at $x = 2$ cm (front view opposite to source). Optical properties: $\mu_s = 10$ cm^{-1}, $\mu_a = 0.01$ cm^{-1}, $g = 0$, $n_m = 1$. Two absorbers ($\mu_a = 2$ cm^{-1}) with diameter 0.6 cm were placed at $(x,y) = (1,0.5)$ and $(x,y) = (1,1.5)$.

(a) σ_M^ϕ of diffusion solution.
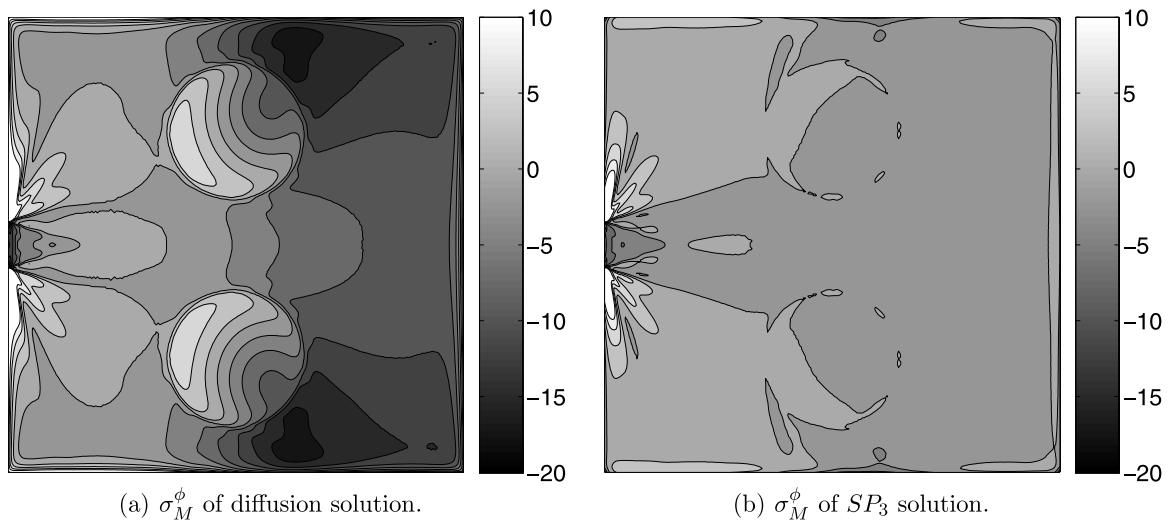
(b) σ_M^ϕ of SP_3 solution.

Fig. 18. Case 14: 2-D spatial distribution of model error σ_M^ϕ in (%) of fluence derived from (a) diffusion solution and (b) SP_3 solution with respect to fluence of S_6 solution. Source position is at the center on the left-hand side. Optical properties: $\mu_s = 10$ cm^{-1}, $\mu_a = 0.01$ cm^{-1}, $g = 0$, $n_m = 1$. Two absorbers ($\mu_a = 2$ cm^{-1}) with diameter 0.6 cm were placed at $(x,y) = (1,0.5)$ and $(x,y) = (1,1.5)$.

6.3. Diffusive medium with highly absorbing inclusions

We also considered a diffusive medium with size of 2 cm × 2 cm containing small highly absorbing domains. The optical parameters of the bulk medium were $\mu_s = 10$ cm^{-1}, $g = 0$, $\mu_a = 0.01$ cm^{-1}, and $n_m = 1$. The reduced scattering and absorption coefficients are typical for wavelengths in the near-infrared range ($\mu_s' \gg \mu_a$). We have embedded a single absorbing object in case 13 at position $(x,y) = (1,1)$ and two absorbing objects in case 14 at positions $(x,y) = (1,0.5)$ and $(x,y) = (1,1.5)$. All circular inclusions have a diameter of 0.6 cm. The absorption coefficient was $\mu_a = 2$ cm^{-1} for the inclusions, representing a highly vascularized tissue with strong light absorption. These tissue types can be found e.g. in the liver and heart of small animals.

Table 2
Total model error σ_M^ϕ of fluence in (%) for the diffusion (P_1), SP_3, SP_5, and SP_7 solution with respect to the S_{16} transport solution

Case #	μ_s (cm^{-1})	g (n.u.)	μ_a (cm^{-1})	n_m (n.u.)	$\sigma_M^\phi(P_1)$ (%)	$\sigma_M^\phi(SP_3)$ (%)	$\sigma_M^\phi(SP_5)$ (%)	$\sigma_M^\phi(SP_7)$ (%)
1	10	0	0.01	1	1.73	1.45	1.51	1.51
2	10	0	0.01	1.37	6.22	2.40	2.08	1.51
3	20	0.5	0.01	1.37	4.30	2.83	2.05	0.88
4	50	0.8	0.01	1.37	3.36	2.44	2.05	1.24
5	10	0	1	1	6.26	2.69	2.80	2.81
6	20	0.5	2	1.37	10.68	4.18	3.97	2.93

Medium size is 1 cm × 1 cm.

Table 3
Total model error $\sigma_M^{J^+}$ of partial current in (%) for the diffusion (P_1), SP_3, SP_5, and SP_7 solution with respect to the S_{16} transport solution

Case #	μ_s (cm^{-1})	g (n.u.)	μ_a (cm^{-1})	n_m (n.u.)	$\sigma_M^{J^+}(P_1)$ (%)	$\sigma_M^{J^+}(SP_3)$ (%)	$\sigma_M^{J^+}(SP_5)$ (%)	$\sigma_M^{J^+}(SP_7)$ (%)
1	10	0	0.01	1	0.70	0.33	0.47	0.53
2	10	0	0.01	1.37	5.02	1.67	1.67	1.39
3	20	0.5	0.01	1.37	3.50	1.66	1.67	1.67
4	50	0.8	0.01	1.37	1.14	2.70	2.54	0.91
5	10	0	1	1	15.53	2.60	2.97	3.11
6	20	0.5	2	1.37	30.11	3.04	3.10	2.23

Medium size is 1 cm × 1 cm.

Table 4
Relative processing time T for completing a numerical calculation of the SP_N and S_N methods with respect to the processing time for the diffusion calculation

Case #	μ_s (cm^{-1})	g (n.u.)	μ_a (cm^{-1})	n_m (n.u.)	$T(SP_3)$ (n.u.)	$T(SP_5)$ (n.u.)	$T(SP_7)$ (n.u.)	$T(S_{16}^{DD})$ (n.u.)	$T(S_{16}^{SD})$ (n.u.)
1	10	0	0.01	1	2.52	5.06	10.12	17.88	681.32
2	10	0	0.01	1.37	2.41	4.93	9.86	18.88	734.13
3	20	0.5	0.01	1.37	2.43	4.94	9.88	34.73	1370.52
4	50	0.8	0.01	1.37	2.42	4.94	9.87	77.94	3442.55
5	10	0	1	1	2.60	5.21	10.44	17.73*	644.41
6	20	0.5	2	1.37	2.78	5.27	10.97	35.65*	1519.01

$T(S_{16}^{DD})$ constitutes the relative processing time of the S_{16} method with DD scheme on a 121 × 121 grid, and $T(S_{16}^{SD})$ is the processing time used by of the S_{16} method with SD scheme on a 721 × 721 grid. *Note*: The S_{16} DD method yields oscillating solutions with large discretization errors.

Table 5
Total model error σ_M^ϕ of fluence in (%) for the diffusion (P_1), SP_3, SP_5, and SP_7 solutions on 241 × 241 grid with respect to the S_6 transport solution on 1441 × 1441 grid (cases 10–12)

Case #	μ_s (cm^{-1})	g (n.u.)	μ_a (cm^{-1})	n_m (n.u.)	$\sigma_M^\phi(P_1)$ (%)	$\sigma_M^\phi(SP_3)$ (%)	$\sigma_M^\phi(SP_5)$ (%)	$\sigma_M^\phi(SP_7)$ (%)
7	10	0	0.01	1	0.85	0.65	0.62	0.60
8	10	0	0.01	1.37	3.86	4.07	3.74	1.39
9	20	0.5	0.01	1.37	2.41	2.88	2.42	0.81
10	10	0	0.5	1	6.22	2.31	2.43	2.48
11	10	0	1	1	14.96	2.62	2.55	2.53
12	10	0	2	1	38.99	4.40	4.19	4.20

Cases 7–9 consider SP_N and diffusion solutions on the 121 × 121 grid, and S_{16} solutions on the 721 × 721 grid. Medium size is 2 cm × 2 cm.

Case 13 demonstrates the impact of a single highly absorbing inclusion inside a diffusive medium on the fluence and partial current. We anticipated similar results as in case 7 with uniform distribution of optical parameters. We observe a good match between the SP_N and S_6 solutions, but a relatively large model error of the diffusion solution, due to the elevated absorption of the embedded inclusion. Fig. 15 shows the model

Table 6
Total model error $\sigma_M^{J^+}$ of partial current in (%) for the diffusion (P_1), SP_3, SP_5, and SP_7 solution on 241×241 grid with respect to the S_6 transport solution on 1441×1441 grid (cases 10–11)

Case #	μ_s (cm^{-1})	g (n.u.)	μ_a (cm^{-1})	n_m (n.u.)	$\sigma_M^{J^+}(P_1)$ (%)	$\sigma_M^{J^+}(SP_3)$ (%)	$\sigma_M^{J^+}(SP_5)$ (%)	$\sigma_M^{J^+}(SP_7)$ (%)
7	10	0	0.01	1	0.88	0.22	0.12	0.08
8	10	0	0.01	1.37	3.45	2.75	2.66	0.44
9	20	0.5	0.01	1.37	1.79	2.24	1.98	0.19
10	10	0	0.5	1	11.24	0.71	1.00	1.11
11	10	0	1	1	32.18	2.73	3.01	3.14
12	10	0	2	1	67.43	6.86	6.32	6.45

Cases 7–9 consider SP_N and diffusion solutions on the 121×121 grid, and S_{16} solutions on the 721×721 grid. Medium size is $2\,cm \times 2\,cm$.

Table 7
Relative processing time T for completing a numerical calculation of the SP_N methods, S_{16} method with DD or SD scheme, and S_6 method with SD scheme with respect to the processing time for the diffusion calculation

Case #	μ_s (cm^{-1})	g (n.u.)	μ_a (cm^{-1})	n_m (n.u.)	$T(SP_3)$ (n.u.)	$T(SP_5)$ (n.u.)	$T(SP_7)$ (n.u.)	$T(S_{16}^{DD})$ (n.u.)	$T(S_{16}^{SD})$ (n.u.)	$T(S_6^{SD})$ (n.u.)
7	10	0	0.01	1	2.51	5.03	10.08	41.93	2091.34	–
8	10	0	0.01	1.37	2.35	4.83	8.61	45.91	2343.54	–
9	20	0.5	0.01	1.37	2.37	4.85	8.63	86.23	4512.51	–
10	10	0	0.5	1	2.55	5.11	10.22	5.87*	–	31.98
11	10	0	1	1	2.60	5.22	10.44	5.84*	–	31.17
12	10	0	2	1	2.71	5.43	10.87	6.09*	–	31.76

The diffusion, SP_N, and S_{16} (DD scheme) calculations are performed either on a 241×241 grid (cases 10–12), or on a 121×121 grid (cases 7–9). The S_{16} calculations with SD scheme were performed on a 721×721 grid (cases 7–9), whereas the S_6 calculations were performed on the 1441×1441 grid (cases 10–12). *Note: S_{16} method with DD scheme yields oscillating solutions with partially large discretization errors σ_E.

error $\sigma_M^{J^+}$ of the partial current at the medium boundaries along the x-axis (side view) and y-axis (front view) opposite to the source). Fig. 16 displays the spatial distribution of the model errors σ_M^ϕ within the x–y plane inside the medium of the diffusion and SP_3 solutions. We found an increased model error σ_M^ϕ of the diffusion solution at the location of the absorber and on the rear site of the medium, being in the "shadow" of the absorber. The SP_3 solution shows a relatively small deviation from the transport solution. The same observation holds in case 14 for the fluence (Fig. 18) and partial current (Fig. 17). Two highly absorbing inclusions further increase the model error of the diffusion solution as seen in Fig. 18. However, the solutions of the SP_N methods are in relatively good agreement with the S_6 transport solution.

7. Discussion

We have derived the SP_N equations up to order $N = 7$ from the equation of radiative transfer for anisotropically scattering biological tissue with partially-reflective boundary conditions. Our numerical study for validating the derived SP_N equations has focused on scattering media less than 22 tmfp thick. Accurate modeling of light propagation in small tissue geometries is relevant in small animal imaging, an imaging modality that has gained increased attention in recent years. Furthermore, we have considered optical parameters at wavelengths ranging from the near-infrared to the visible region.

We derived the SP_N equations and boundary conditions by employing a formal approach. The resulting SP_N equations are coupled diffusion equations, which we numerically solved. We made several observations concerning the accuracy of the SP_N solutions, in comparison to the S_N benchmark solutions. We considered the impact of partially-reflective boundary conditions, large absorption, and anisotropic scattering on the SP_N solutions.

Our first observation is that all SP_N, diffusion, and S_N solutions are in good agreement for a diffusive regime with non-reentry boundary conditions ($n_m = 1$). This can be seen for cases 1 and 7, having optical parameters of $\mu_s = 10$ cm^{-1} and $\mu_a = 0.01$ cm^{-1}. We observed for case 7 an average model error of the fluence

of less than $\sigma_M^\phi < 0.65\%$ for all SP_N solutions, and a model error of $\sigma_M^\phi = 0.85\%$ for the diffusion solution. The model error of the partial current was less than $\sigma_M^{J^+} < 0.22\%$ for the SP_N solutions and $\sigma_M^{J^+} = 0.88\%$ for the diffusion solution. Similar results were obtained from the small medium (case 1: 1 cm × 1 cm) with same optical parameters. Our observation is consistent with the theoretical expectation that P_1 and SP_N solutions should agree well with the transport solution in diffusive regimes. Based on these findings, we became confident that our numerical implementations of all methods were correct.

However, we found that the diffusion solution significantly deviates from the S_N transport solution in near-boundary domains, with distances of less than two tmfp from the medium–air interface. The model error of the diffusion solution is approximately up to five times larger (cases 2 and 3 in Figs. 4 and 5) than the model error inside the bulk medium, even when the diffusion condition $\mu_s' \gg \mu_a$ holds. In contrast, SP_N methods yield more accurate results for the fluence ϕ in near-boundary subdomains. We did not observe a significantly increased model error for SP_N solutions in these subdomains.

Our second observation concerns the impact of partially-reflective boundary conditions on the model error. Partially-reflective boundary conditions, due to a refractive index mismatch ($n_m > 1$) between the air–tissue interface, influence not only the partial current J^+ at the boundary, but also the fluence distribution deep inside the medium. In general, the model error of all solutions increased when using partially reflective boundaries, as can be seen for example in case 2 ($n_m = 1.37$). When compared to case 1 ($n_m = 1$), we found an increase of σ_M^ϕ up to 2.40% for the fluence and of $\sigma_M^{J^+}$ up to 1.67% for the partial current of the SP_3 method. The model error decreased for $N > 3$ and was smallest for the SP_7 solution with $\sigma_M^\phi = 1.51\%$ and $\sigma_M^{J^+} = 1.39\%$. The model error of the diffusion solution was 6.22% and 5.02%, in average four times larger than the error of the SP_7 method. This result confirms that SP_N methods describe partially reflective boundary conditions more accurately than the diffusion method.

In our numerical study, we did not take into account the refractive index mismatch of interfaces between tissue domains with different scattering and absorption coefficients. For example, in cases 13 and 14 we did not model partial reflectance of light between the interfaces of the high-absorbing domain and the background medium. Also, the boundary source did not model the partial-entrance of light due to $R > 0$ for cases with refractive index mismatch $n_m > 1$. And last, we considered only isotropic boundary sources in all cases and no collimated sources. The SP_N methods provide a convenient framework for modeling collimated boundary sources by using a direction-dependent source function $S(\Omega)$ in Eqs. (28). Including this physics will significantly increase the effect of boundary layers on the problem and should measurably improve the SP_N solutions in comparison to the diffusion solutions. However, the extension of our SP_N methods with the mentioned additional physics will be left for future work.

Our third observation concerns the impact of large absorption coefficients μ_a on the light propagation models. Our numerical study clearly shows that the SP_N approximation is more transport-like in highly absorbing tissue media than the diffusion approximation. We considered two different groups of cases: (i) non-diffusive media mimicking highly absorbing tissue at visible wavelengths of $\lambda < 600$ nm (cases 5, 6, 10, 11, and 12), and (ii) tissue-like media with diffusive properties at red and near-infrared wavelengths of $\lambda > 600$ nm, but with highly absorbing non-diffusive subdomains (cases 13 and 14). Regarding the first group of cases, we found that the model error of the fluence of the SP_N methods is less than $\sigma_M^\phi = 2.48\%$ for $\mu_a = 0.5$ cm^{-1} and medium size 2 cm × 2 cm (case 10). For stronger light absorption, such as $\mu_a = 1$ cm^{-1} and $\mu_a = 2$ cm^{-1} (cases 11 and 12), we obtained model errors σ_M^ϕ of only 2.62% and 4.40%, compared to 14.96% and 38.99% for the diffusion solution. The model error $\sigma_M^{J^+}$ of the partial current increased by a factor of two for the diffusion solutions – we found 11.24%, 32.18%, and 67.43% for absorption coefficients $\mu_a = 0.5$ cm^{-1}, $\mu_a = 1$ cm^{-1}, and $\mu_a = 2$ cm^{-1}. Surprisingly, the smallest model error $\sigma_M^{J^+}$ of all SP_N methods was given in some cases by the SP_3 solution: 0.71% and 2.73%. Concerning the second group, when modeling light propagation in diffusive domains with highly absorbing subdomains, we found a model error of the fluence of less than 1.26% for the SP_N methods, whereas the model error of the diffusion equation amounted up to 6.65%. The model error $\sigma_M^{J^+}$ of the partial current for the SP_N methods was always less than 1.7%, but the error of the diffusion solution was 8.73%. In conclusion, the SP_N methods yielded solutions with smallest error when non-diffusive or partially non-diffusive domains were considered. The model error of the diffusion solutions, such as in case 12 with $\sigma_M^{J^+} = 67.43\%$, are unacceptable for accurately modeling light propagation in highly absorbing media.

Solutions of the discrete ordinates approximation to the ERT suffer from ray effects, which are mainly present in highly absorbing media or in the vicinity of sources. We observed ray effects in almost all S_{16} and S_6 solutions in the proximity of the boundary source (see Figs. 16 and 18). The SP_N equations are rotationally invariant and are free of ray effects. Therefore, SP_N methods can be applied to highly absorbing tissue at visible wavelengths, where ray effects decrease the accuracy of the fluence and partial current in S_N solutions.

Our fourth observation concerns the impact of anisotropic scattering on the SP_N approximations. We found that all SP_N solutions in cases 3, 4, 6, and 9 had model errors of less than 3% for the fluence and partial current, which decreased down to 1% with increased N. Moreover, we found that the ERT could be replaced by the simpler isotropically-scattering ERT (Eq. (39)) in cases of low-absorbing and diffusive media with more than 10 tmfp (cases 4 and 9). Both ERTs yield similar solutions as shown in Figs. 6 and 11. Furthermore, the SP_N and diffusion solutions are in good agreement with the S_N solutions.

However, when non-diffusive media with high absorption and anisotropic scattering are considered, the SP_N equations yield significantly more accurate results than either the diffusion solution, or the S_N solutions of the isotropically-scattering ERT (Eq. (39)); see Fig. 8. Thus, in cases of strong tissue absorption, anisotropic scattering must be modeled very accurately, and the diffusion equation is not an adequate approximation anymore. Future studies still need to be carried out, to estimate the impact of modeling of anisotropic scattering in media with optical thickness of less than 10 tmfp and forward-peaked boundary sources. We anticipate an increased model error for the diffusion solution, but smaller deviations of the SP_N solutions from the S_N transport solutions.

Our last important observation concerns the processing time needed to complete a full light propagation calculation. We compared the relative processing times of the SP_N and S_N methods with respect to the diffusion method. The SP_N and diffusion models used the same numerical solvers (Gauss–Seidel method). Hence, being consistent with the numerical solvers, we could objectively quantify the processing time needed for solving the model equations independent of a particular numerical solution technique. We found that the SP_3, SP_5, and SP_7 methods are, respectively, about 2.5, 5, and 10 times more computationally demanding than the diffusion equation. Thus, a transport-like SP_N solution can be achieved while only requiring only 2.5–10 times the computational processing time of the diffusion method.

Our S_N method with SD scheme on fine Cartesian grids was approximately 700–4500 times slower than the diffusion method. The S_N method with the DD scheme on coarse Cartesian grids was 40–80 times slower than the diffusion method for tissue optics problems, but did not always yield physically meaningful solutions when large absorption was considered [42,44].

However, we cannot directly compare the processing speed of our S_N transport method to the processing time needed by the SP_N and diffusion models as an objective measure for computational performance. Our S_N method, which was specifically developed for tissue optics, is not optimized for a time-efficient computation. Therefore, our S_N method is inherently much slower than other more computationally efficient transport techniques as widely employed in nuclear engineering. In nuclear engineering, an optimized S_N technique with diffusion-synthetic acceleration (DSA) is still much slower than an optimized diffusion method. Although the slowdown is problem-dependent, for large 3-D problems, a slowdown of 25–50 is typical. However, these are neutronics problems, for which the quadrature set is usually S_6 or S_8. For the S_{16} quadrature set, the number of ordinates is at least quadrupled, so the cost of solving the ERT is quadrupled. Moreover, it is well known that DSA becomes less efficient when the scattering becomes more forward-peaked. Thus, if one estimates the entire cost of a large tissue optics calculation as compared to the cost of a neutron transport calculation on the same Cartesian grid, a factor of eight increase in cost for the tissue optics problem is reasonable – and is probably low. Applying this factor of 8, we obtain the conservative estimate that for tissue optics problems, an optimized S_N code will be about 200–400 times slower than an optimized diffusion code. This estimate is lower than the slowdown that we observe with our S_N method with SD scheme, but it is still very large, and it argues strongly that even for optimized codes, S_N will be at least 100 times more expensive than low-order SP_N methods.

In conclusion, we have derived a system of diffusion-like SP_N equations that approximate the equation of radiative transfer in tissue-like domains. We have demonstrated in numerical simulations that the SP_N approach, unlike the diffusion method, captures most of the transport properties of biological tissue. We

recommend using the SP_3 method for many tissue optics problems, because it yields transport-like solutions with lowest computational cost, especially for highly-absorbing media. SP_5 and SP_7 solutions exhibit a further improvement in accuracy, but with an increased expense of processing time. SP_7 methods show best results for anisotropically-scattering media with partial-reflection at boundaries. Overall, SP_N methods promise to become a powerful light propagation model for tomographic imaging of biological tissue at wavelengths in the visible region with high tissue absorption. This is particularly important for optical molecular imaging of fluorescent proteins and luciferases, which emit light at visible wavelengths. Furthermore, whole-body tomographic imaging of small animals at near-infrared wavelengths could be improved when highly vascularized tissues with large absorption coefficients, e.g. liver, heart, and kidneys and their tissue vicinities, are imaged. SP_N methods can achieve transport-like solutions at a cost of only a few diffusion calculations, but several orders of magnitude faster than full S_N transport solutions. Therefore, SP_N methods are well-suited for tomographic imaging schemes, where image reconstruction codes repetitively employ light propagation calculations.

Appendix A

A.1. Legendre polynomials

$$
\begin{aligned}
&P_0(\omega) = 1, \\
&P_1(\omega) = \omega, \\
&P_2(\omega) = \frac{1}{2}\left(3\omega^2 - 1\right), \\
&P_3(\omega) = \frac{1}{2}\left(5\omega^3 - 3\omega\right), \\
&P_4(\omega) = \frac{1}{4}\left(\frac{35}{2}\omega^4 - 15\omega^2 + \frac{3}{2}\right), \\
&P_5(\omega) = \frac{1}{4}\left(\frac{63}{2}\omega^5 - 35\omega^3 + \frac{15}{2}\omega\right), \\
&P_6(\omega) = \frac{1}{16}\left(231\omega^6 - 315\omega^4 + 105\omega^2 - 5\right), \\
&P_7(\omega) = \frac{1}{16}\left(429\omega^7 - 693\omega^5 + 315\omega^3 - 35\right).
\end{aligned}
\tag{A.1}
$$

A.2. Boundary coefficients

$$
\begin{aligned}
&A_1 = -R_1, \\
&B_1 = 3R_2, \\
&C_1 = -\frac{3}{2}R_1 + \frac{5}{2}R_3, \\
&D_1 = \frac{3}{2}R_2 - \frac{5}{2}R_4, \\
&E_1 = \frac{15}{8}R_1 - \frac{35}{4}R_3 + \frac{63}{8}R_5, \\
&F_1 = -\frac{15}{8}R_2 + \frac{35}{4}R_4 - \frac{63}{8}R_6, \\
&G_1 = -\frac{35}{16}R_1 + \frac{315}{16}R_3 - \frac{693}{16}R_5 + \frac{429}{16}R_7, \\
&H_1 = \frac{35}{16}R_2 - \frac{315}{16}R_4 + \frac{693}{16}R_6 - \frac{429}{16}R_8,
\end{aligned}
\tag{A.2}
$$

$$A_2 = -\frac{9}{4}R_1 + \frac{15}{2}R_3 - \frac{25}{4}R_5,$$

$$B_2 = \frac{63}{4}R_2 - \frac{105}{2}R_4 + \frac{175}{4}R_6,$$

$$C_2 = -\frac{3}{2}R_1 + \frac{5}{2}R_3,$$

$$D_2 = \frac{3}{2}R_2 - \frac{5}{2}R_4,$$

$$E_2 = -\frac{45}{16}R_1 + \frac{285}{16}R_3 - \frac{539}{16}R_5 + \frac{315}{16}R_7,$$

$$F_2 = \frac{45}{16}R_2 - \frac{285}{16}R_4 + \frac{539}{16}R_6 - \frac{315}{16}R_8,$$

$$G_2 = \frac{105}{32}R_1 - 35R_3 + \frac{1827}{16}R_5 - \frac{297}{2}R_7 + \frac{2145}{32}R_9,$$

$$H_2 = -\frac{105}{32}R_2 + 35R_4 - \frac{1827}{16}R_6 + \frac{297}{2}R_8 - \frac{2145}{32}R_{10},$$

(A.3)

$$A_3 = -\frac{225}{64}R_1 + \frac{525}{16}R_3 - \frac{3395}{32}R_5 + \frac{2205}{16}R_7 - \frac{3969}{64}R_9,$$

$$B_3 = \frac{2475}{64}R_2 - \frac{5775}{16}R_4 + \frac{37345}{32}R_6 - \frac{24255}{16}R_8 + \frac{43659}{64}R_{10},$$

$$C_3 = \frac{15}{8}R_1 - \frac{35}{4}R_3 + \frac{63}{8}R_5,$$

$$D_3 = -\frac{15}{8}R_2 + \frac{35}{4}R_4 - \frac{63}{8}R_6,$$

$$E_3 = -\frac{45}{16}R_1 + \frac{285}{16}R_3 - \frac{539}{16}R_5 + \frac{315}{16}R_7,$$

$$F_3 = \frac{45}{16}R_2 - \frac{285}{16}R_4 + \frac{539}{16}R_6 - \frac{315}{16}R_8,$$

$$G_3 = -\frac{525}{128}R_1 + \frac{7175}{128}R_3 - \frac{17325}{64}R_5 + \frac{37395}{64}R_7 - \frac{73689}{128}R_9 + \frac{27027}{128}R_{11},$$

$$H_3 = \frac{525}{128}R_2 - \frac{7175}{128}R_4 + \frac{17325}{64}R_6 - \frac{37395}{64}R_8 + \frac{73689}{128}R_{10} - \frac{27027}{128}R_{12},$$

(A.4)

$$A_4 = -\frac{1225}{256}R_1 + \frac{11025}{128}R_3 - \frac{147735}{256}R_5 + \frac{116655}{64}R_7 - \frac{750519}{256}R_9 + \frac{297297}{128}R_{11} - \frac{184041}{256}R_{13},$$

$$B_4 = 15\left(\frac{1225}{256}R_2 - \frac{11025}{128}R_4 + \frac{147735}{256}R_6 - \frac{116655}{64}R_8 + \frac{750519}{256}R_{10} - \frac{297297}{128}R_{12} + \frac{184041}{256}R_{14}\right),$$

$$C_4 = -\frac{35}{16}R_1 + \frac{315}{16}R_3 - \frac{693}{16}R_5 + \frac{429}{16}R_7,$$

$$D_4 = \frac{35}{16}R_2 - \frac{315}{16}R_4 + \frac{693}{16}R_6 - \frac{429}{16}R_8,$$

$$E_4 = \frac{105}{32}R_1 - 35R_3 + \frac{1827}{16}R_5 - \frac{297}{2}R_7 + \frac{2145}{32}R_9,$$

$$F_4 = -\frac{105}{32}R_2 + 35R_4 - \frac{1827}{16}R_6 + \frac{297}{2}R_8 - \frac{2145}{32}R_{10},$$

$$G_4 = -\frac{525}{128}R_1 + \frac{7175}{128}R_3 - \frac{17325}{64}R_5 + \frac{37395}{64}R_7 - \frac{73689}{128}R_9 + \frac{27027}{128}R_{11},$$

$$H_4 = \frac{525}{128}R_2 - \frac{7175}{128}R_4 + \frac{17325}{64}R_6 - \frac{37395}{64}R_8 + \frac{73689}{128}R_{10} - \frac{27027}{128}R_{12}.$$

(A.5)

A.3. Coefficients for partial current

$$J_0 = -\frac{1}{2}R_1,$$

$$J_1 = -\frac{3}{2}R_2,$$

$$J_2 = \frac{5}{4}R_1 - \frac{15}{4}R_3,$$

$$J_3 = \frac{21}{4}R_2 - \frac{35}{4}R_4,$$

$$J_4 = -\frac{27}{16}R_1 + \frac{135}{8}R_3 - \frac{315}{16}R_5,$$

$$J_5 = -\frac{165}{16}R_2 + \frac{385}{8}R_4 - \frac{693}{16}R_6,$$

$$J_6 = \frac{65}{32}R_1 - \frac{1365}{32}R_3 + \frac{4095}{32}R_5 - \frac{3003}{32}R_7,$$

$$J_7 = \frac{525}{32}R_2 - \frac{4725}{32}R_4 + \frac{10395}{32}R_6 - \frac{6435}{32}R_8.$$

$$(A.6)$$

References

[1] A.P. Gibson, J.C. Hebden, S.R. Arridge, Recent advances in diffuse optical imaging, Phys. Med. Biol. 50 (2005) R1–R43.

[2] A.Y. Bluestone, G. Abdoulaev, C. Schmitz, R.L. Barbour, A.H. Hielscher, Three-dimensional optical tomography of hemodynamics in the human head, Opt. Exp. 9 (6) (2001) 272–286.

[3] A.H. Hielscher, A.D. Klose, A.K. Scheel, B. Moa-Anderson, M. Backhaus, U. Netz, J. Beuthan, Sagittal laser optical tomography for imaging of rheumatoid finger joints, Phys. Med. Biol. 49 (2004) 1147–1163.

[4] A.H. Hielscher, Optical tomographic imaging of small animals, Curr. Opin. Biotechnol. 16 (2005) 79–88.

[5] R. Weissleder, U. Mahmood, Molecular imaging, Radiology 219 (2001) 316–333.

[6] A.J. Welch, M.J.C. van Gemert, Optical-Thermal Response of Laser-Irradiated Tissue, Plenum Press, New York, 1995.

[7] W.F. Cheong, S.A. Prahl, A.J. Welch, A review of the optical properties of biological tissue, IEEE J. Quantum Electron. 26 (1990) 2166–2185.

[8] V. Tuchin, Tissue Optics, SPIE, Bellingham, WA, 2000.

[9] A.H. Hielscher, R.E. Alcouffe, R.L. Barbour, Comparison of finite-difference transport and diffusion calculations for photon migration in homogeneous and heterogeneous tissues, Phys. Med. Biol. 43 (1998) 1285–1302.

[10] E.D. Aydin, C.R.E. de Oliveira, A.J.H. Goddard, A comparison between transport and diffusion calculations using a finite element-spherical harmonics radiation transport method, Med. Phys. 29 (9) (2002) 2013–2023.

[11] B.W. Rice, M.D. Cable, M.B. Nelson, In vivo imaging of light-emitting probes, J. Biomed. Opt. 6 (4) (2001) 432–440.

[12] T. Troy, D. Jekic-McMullen, L. Sambucetti, B. Rice, Quantitative comparison of the sensitivity of detection of fluorescent and bioluminescent reporters in animal models, Mol. Imaging 3 (1) (2004) 9–23.

[13] V.R. Viviani, T.L. Oehlmeyer, F.G.C. Arnoldi, M.R. Brochetto-Braga, A new firefly luciferase with bimodal spectrum: identification of structural determinants of spectral pH-sensitivity in firefly luciferases, Photochem. Photobiol. 81 (2005) 843–848.

[14] H. Zhao, T.C. Doyle, O. Coquoz, F. Kalish, B. Rice, C.H. Contag, Emission spectra of bioluminescent reporters and interaction with mammalian tissue determine the sensitivity of detection in vivo, J. Biomed. Opt. 10 (4) (2005) 041210-1–041210-9.

[15] K.M. Case, P.F. Zweifel, Linear Transport Theory, Addison-Wesley, Reading, MA, 1967.

[16] M.L. Adams, E.W. Larsen, Fast iterative methods for discrete-ordinates particle transport calculations, Prog. Nucl. Energy 40 (1) (2002) 3–159.

[17] J.K. Fletcher, The solution of the multigroup neutron transport equation using spherical harmonics, Nucl. Sci. Eng. 84 (1983) 33–46.

[18] K. Kobayashi, H. Oigawa, H. Yamagata, The spherical harmonics method for the multigroup transport equations in x–y geometry, Ann. Nucl. Energy 13 (12) (1986) 663–678.

[19] A.D. Klose, V. Ntziachristos, A.H. Hielscher, The inverse source problem based on the radiative transfer equation in optical molecular imaging, J. Comput. Phys. 202 (2005) 323–345.

[20] E.M. Gelbard, Application of spherical harmonics methods to reactor problems, WAPD-BT-20, Bettis Atomic Power Laboratory, 1960.

[21] E.M. Gelbard, J. Davis, J. Pearson, Iterative solutions to the P_1 and double P_1 equations, Nucl. Sci. Eng. 5 (1959) 36–44.

[22] D.I. Tomasevic, E.W. Larsen, The simplified P_2 approximation, Nucl. Sci. Eng. 122 (1996) 309–325.

[23] E.W. Larsen, J.E. Morel, J.M. McGhee, Asymptotic derivation of the multigroup P1 and simplified P_N equations with anisotropic scattering, Nucl. Sci. Eng. 123 (1996) 328.

[24] R.T. Ackroyd, C.R.E. de Oliveira, A. Zolfaghari, A.J.H. Goddard, On a rigorous resolution of the transport equation into a system of diffusion-like equations, Prog. Nucl. Eng. 35 (1) (1999) 1–64.
[25] P.S. Brantley, E.W. Larsen, The simplified P3 approximation, Nucl. Sci. Eng. 134 (2000) 1–21.
[26] J.E. Morel, J.M. McGhee, E.W. Larsen, A three-dimensional time-dependent unstructured tetrahedral-mesh SP_N method, Nucl. Sci. Eng. 123 (1996) 319–327.
[27] P. Kotiluoto, Fast tree multigrid transport application for the simplified P_3 approximation, Nucl. Sci. Eng. 138 (2001) 269–278.
[28] P. Kotiluoto, P. Hiismäki, Application of the new MultiTrans SP_3 radiation transport code in BNCT dose planning, Med. Phys. 28 (9) (2001) 1905–1910.
[29] R. Ciolini, G.G.M. Coppa, B. Montagnini, P. Ravetto, Simplified P_N and A_N methods in neutron transport, Prog. Nucl. Energy 40 (2) (2002) 237–264.
[30] J.A. Josef, J.E. Morel, Simplified spherical harmonic method for coupled electron–photon transport calculations, Phys. Rev. E 57 (5) (1998) 6161–6171.
[31] E.W. Larsen, G. Thoemmes, A. Klar, M. Deaid, T. Goetz, Simplified P_N approximations to the equations of radiative heat transfer and applications, J. Comput. Phys. 183 (2002) 652–675.
[32] M. Lemanska, On the simplified P_n method in the 2-D diffusion code EXTERMINATOR, Atomkernenergie 37 (1981) 173–175.
[33] E.E. Lewis, G. Palmiotti, Simplified spherical harmonics in the variational nodal method, Nucl. Sci. Eng. 126 (1997) 48–58.
[34] A. Kienle, F.K. Forster, R. Hibst, Influence of the phase function on determination of the optical properties of biological tissue by spatially resolved reflectance, Opt. Lett. 26 (20) (2001) 1571–1573.
[35] S.K. Sharma, S. Banerjee, Role of approximate phase functions in Monte Carlo simulation of light propagation in tissues, J. Opt. A 5 (2003) 294–302.
[36] R.E. Marshak, Note on the spherical harmonic method as applied to the Milne problem for a sphere, Phys. Rev. 71 (7) (1947) 443–446.
[37] M. Keijzer, W.M. Star, P.R.M. Storchi, Optical diffusion in layered media, Appl. Opt. 27 (9) (1988) 1820–1824.
[38] R.C. Haskell, L.O. Svaasand, T.-T. Tsay, T.-C. Feng, M.S. McAdams, B.J. Tromberg, Boundary conditions for the diffusion equation in radiative transfer, J. Opt. Soc. Am. A 11 (10) (1994) 2727–2741.
[39] T. Spott, L.O. Svaasand, Collimated light sources in the diffusion approximation, Appl. Opt. 39 (34) (2000) 6453–6465.
[40] W.H. Press, S.A. Teukolsky, W.T. Vetterling, B.P. Flannery, Numerical Recipes in C: The Art of Scientific Computing, second ed., Cambridge University Press, Cambridge, 1994.
[41] K.W. Morton, D.F. Mayers, Numerical Solution of Partial Differential Equations, Cambridge University Press, Cambridge, 1994.
[42] K.D. Lathrop, Spatial differencing of the transport equation: positivity vs. accuracy, J. Comput. Phys. 4 (1969) 475–498.
[43] J.J. Duderstadt, W.R. Martin, Transport Theory, Wiley, New York, 1979.
[44] D. Lacroix, N. Berour, P. Boulet, G. Jeandel, Transient radiative and conductive heat transfer in non-gray semitransparent two-dimensional media with mixed boundary conditions, Heat Mass Transfer 42 (2006) 322–337.
[45] A.Y. Bluestone, M. Stewart, B. Lei, I.S. Kass, J. Lasker, G.S. Abdoulaev, A.H. Hielscher, Three-dimensional optical tomographic brain imaging in small animals, Part I: Hypercapnia, J. Biomed. Opt. 9 (5) (2004) 1046–1062.
[46] A.Y. Bluestone, M. Stewart, J. Lasker, G.S. Abdoulaev, A.H. Hielscher, Three-dimensional optical tomographic brain imaging in small animals, Part II: Unilateral Carotid Occlusion, J. Biomed. Opt. 9 (5) (2004) 1063–1073.